HHS Public Access

Author manuscript

Cell. Author manuscript; available in PMC 2021 April 16.

Published in final edited form as:

Cell. 2020 April 16; 181(2): 410–423.e17. doi:10.1016/j.cell.2020.02.055.

Functionally Distinct Neuronal Ensembles Within the Memory Engram

Xiaochen Sun[1,2,3], **Max J. Bernstein**[1], **Meizhen Meng**[1,8], **Siyuan Rao**[1,4], **Andreas T. Sørensen**[1,5], **Li Yao**[6], **Xiaohui Zhang**[6], **Polina O. Anikeeva**[1,4,7], **Yingxi Lin**[1,2,8,9,*]

[1]McGovern Institute for Brain Research, Massachusetts Institute of Technology, Cambridge, MA 02139, USA.

[2]Department of Brain and Cognitive Sciences, Massachusetts Institute of Technology, Cambridge, MA 02139, USA.

[3]Molecular and Cellular Neuroscience Graduate Program, Massachusetts Institute of Technology, Cambridge, MA 02139, USA.

[4]Research Laboratory of Electronics, Massachusetts Institute of Technology, Cambridge, MA 02139, USA.

[5]Present address: Department of Neuroscience, University of Copenhagen, Copenhagen, Denmark.

[6]State Key Laboratory of Cognitive Neuroscience & Learning and IDG/McGovern Institute for Brain Research, Beijing Normal University, Beijing 100875, China.

[7]Department of Materials Science and Engineering, Massachusetts Institute of Technology, Cambridge, MA 02139, USA.

[8]Present address: Department of Psychiatry and Behavioral Sciences, SUNY Upstate Medical University, Syracuse, NY 13078, USA

[9]Lead Contact

Summary:

Memories are believed to be encoded by sparse ensembles of neurons in the brain. However, it remains unclear whether there is functional heterogeneity within individual memory engrams, i.e., if separate neuronal subpopulations encode distinct aspects of the memory and drive memory

*Correspondence: yingxi@mit.edu or linyi@upstate.edu.

Author contributions: X.S. and Y.L. designed the experiments and wrote the manuscript. X.S. performed or participated in all experiments described in the manuscript. M.J.B contributed to surgery, behavior experiments and histological analyses. M.M. contributed to behavior and electrophysiological experiments. S.R. and P.O.A. assisted with fiber photometry experiments. A.T.S. constructed the reporter systems. L.Y. and X.Z. assisted with electrophysiological experiments. Y.L. designed and supervised the study.

Declaration of Interests: The authors have no competing interests.

Supplemental Information

Table S1. Statistical Table, Related to Figures 1, 2, 3, 4, 5, 6, 7, S1, S2, S3, S4, S5, S6, and S7.

expression differently. Here we show that contextual fear memory engrams in the mouse dentate gyrus contain functionally distinct neuronal ensembles, genetically defined by the *Fos*- or *Npas4*-dependent transcriptional pathways. The *Fos*-dependent ensemble promotes memory generalization and receives enhanced excitatory synaptic inputs from the medial entorhinal cortex, which we find itself also mediates generalization. The *Npas4*-dependent ensemble promotes memory discrimination and receives enhanced inhibitory drive from local cholecystokinin-expressing interneurons, the activity of which is required for discrimination. Our study provides causal evidence for functional heterogeneity within the memory engram, and reveals synaptic and circuit mechanisms used by each ensemble to regulate the memory discrimination-generalization balance.

Graphical Abstract

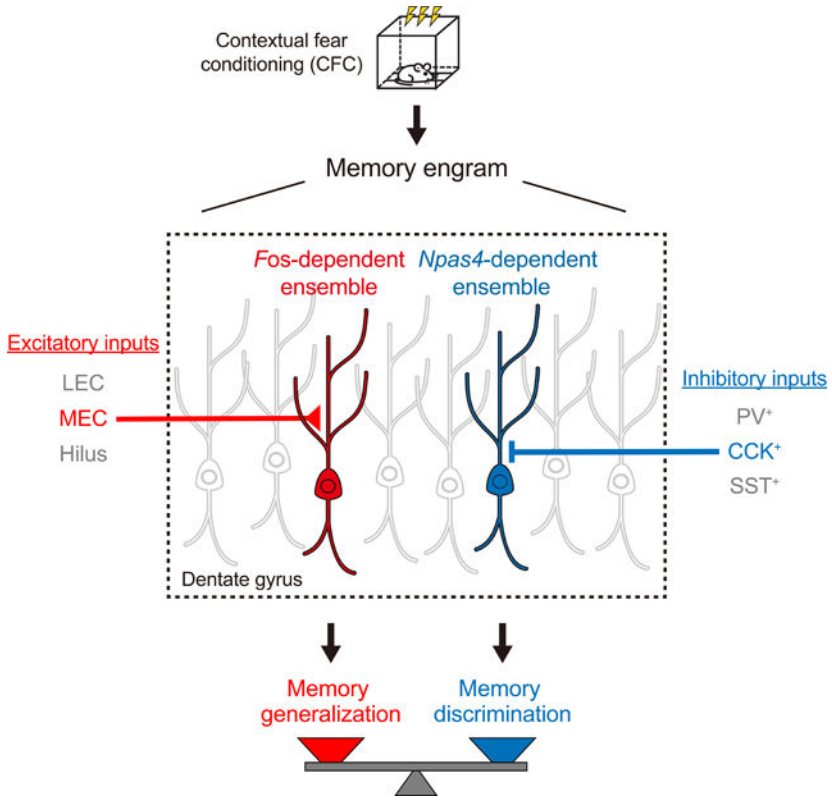

eTOC blurb

Two functionally distinct neuronal ensembles within a single memory engram undergo different learning-induced synaptic modifications and drive memory-guided behaviors in opposite directions.

Keywords

memory engram; heterogeneity; neuronal ensembles; activity-dependent pathways; dentate gyrus; discrimination; generalization

Introduction

Engrams of individual memories are the long-lasting biological changes that take place in the brain to encode specific experiences (Josselyn et al., 2015; Tonegawa et al., 2015). Each engram is thought to contain a sparse population of neurons that are activated by the specific learning experience, undergo long-lasting synaptic modifications (Choi et al., 2018; Ryan et al., 2015), and mediate the expression of the encoded memory (Cai et al., 2016; Han et al., 2009; Liu et al., 2012; Yokose et al., 2017). However, a fundamental question remains: whether neurons within a single memory engram are functionally homogeneous, as generally assumed, or heterogeneous, as hypothesized to allow different aspects of a memory to be individually represented and regulated (Ghandour et al., 2019; Mallory and Giocomo, 2018; Richter et al., 2016; Tanaka and McHugh, 2018). The latter would favor flexible memory expression in an ever-changing environment (Eichenbaum, 2004; Xu and Sudhof, 2013). Indeed, heterogeneous population activities have been observed during learning (Grewe et al., 2017; Grosmark and Buzsáki, 2016; Herry et al., 2008; Tanaka et al., 2018) and are theorized to be critical for efficient information coding (Chelaru and Dragoi, 2008; Osborne et al., 2008). Nevertheless, causal evidence for functional heterogeneity within a single engram is still lacking. It is also unknown whether functionally distinct neuronal ensembles can be distinguished within an engram at the molecular and cellular levels, and if they engage different synaptic and circuit mechanisms to modulate memory-guided adaptive behaviors.

Genetically encoded activity reporters based on immediate early genes (IEGs) such as *Fos*, and *Arc* (Barth, 2007; Kawashima et al., 2014), commonly considered proxies of neuronal activity (Guzowski et al., 2005), have been used to identify neuronal ensembles in engrams. Until now, most studies have focused on ensembles defined by a single activity-dependent pathway (Barth et al., 2004; Denny et al., 2014; Kawashima et al., 2013; Reijmers et al., 2007). However, activity-dependent pathways are known to be highly diverse: they respond differently to external stimuli and mediate distinct cellular and synaptic processes (Yap and Greenberg, 2018). The relationship between ensembles defined by different pathways has not been investigated. It is conceivable that different activity-dependent pathways may define functionally distinct ensembles within engrams, providing the means to genetically dissect them.

Here we directly examine the functionalities of neuronal ensembles defined by two different activity-dependent pathways, downstream of the IEGs *Fos* and *Npas4*, both of which are highly induced by learning but likely trigger distinct synaptic changes in activated neurons (Flavell and Greenberg, 2008; Sun and Lin, 2016). The widely used activity marker *F*os mediates long-term potentiation of excitatory synapses (Fleischmann et al., 2003). *Npas4*, a neuron-specific IEG that is selectively activated by neuronal activity, differs from *Fos* in that it preferentially recruits inhibitory synapses, or sometimes diminishes excitatory synapses, onto excitatory neurons (Lin et al., 2008; Weng et al., 2018). These different synaptic functions of *Fos* and *Npas4* strongly suggest that the ensembles they define may be functionally distinct.

To investigate the functionalities of the *Fos*- and *Npas4*-dependent ensembles, we focus on the dentate gyrus (DG) of the hippocampus and the roles of these ensembles in memory discrimination and generalization, opposed processes that must be balanced appropriately to differentiate between different stimuli (Frankland et al., 1998; Grosso et al., 2018; van Dijk and Fenton, 2018) but also allow recognition of shared features (Dunsmoor and Paz, 2015; Wiltgen and Silva, 2007). The discrimination-generalization balance is critical to adaptive learning and avoiding maladaptive conditions such as post-traumatic stress disorder (PTSD) (Mahan and Ressler, 2012) and panic disorder (Kheirbek et al., 2012). The DG has traditionally been believed to mediate memory discrimination (Leutgeb et al., 2007; McHugh et al., 2007; Treves and Rolls, 1994), but recent studies suggest that this region can also promote memory generalization (Hainmueller and Bartos, 2018; Nakashiba et al., 2012). Very little is known about the involvement of neuronal ensembles in the DG in these processes. Here we show that the *Fos*-and *Npas4*-dependent neuronal ensembles within the DG contextual fear memory engram regulate memory generalization and discrimination, respectively, by engaging distinct synaptic and circuit mechanisms.

Results

Fos- and *Npas4*-dependent RAM (*F*-RAM and *N*-RAM) Reporters

To identify *Fos*- and *Npas4*-dependent ensembles within the engram, we used our RAM reporter system (Sørensen et al., 2016) to create *Fos*-dependent (*F*-RAM) and *Npas4*-dependent (*N*-RAM) RAM reporters. FOS and NPAS4 are transcription factors and exert their functions via their downstream transcriptional targets, so we designed reporters that reflect these transcriptional outputs. The promoters in *F*-RAM and *N*-RAM ($P_{F\text{-RAM}}$ and $P_{N\text{-RAM}}$) consist of the consensus DNA binding sequences for FOS and NPAS4 (Figure S1A). Both promoters drive the expression of reporter genes under the temporal control of a modified doxycycline (Dox)-dependent Tet-Off system developed for the RAM system (Figure 1A).

Both $P_{F\text{-RAM}}$ and $P_{N\text{-RAM}}$ were robustly activated by membrane depolarization in cultured mouse hippocampal neurons (Figure 1B; numerical data and statistical information for all figures are included in Table S1), suggesting that they are regulated by neuronal activity. $P_{F\text{-RAM}}$ was activated by various extracellular stimuli known to activate *Fos*, and $P_{N\text{-RAM}}$ was selectively activated by neuronal activity, recapitulating this unique property of *Npas4* (Lin et al., 2008). Overexpression of *Fos*, but not *Npas4*, drives $P_{F\text{-RAM}}$ activity, whereas overexpression of *Npas4*, but not *Fos*, activates $P_{N\text{-RAM}}$ (Figure 1B), indicating that activation of $P_{F\text{-RAM}}$ and $P_{N\text{-RAM}}$ is selective. Both the *F*-RAM and *N*-RAM reporters showed low background activation and were robustly induced by neuronal activity in a Dox-dependent manner (Figure S1D).

We used AAV-*F*-RAM-mKate2 or AAV-*N*-RAM-mKate2 to label active neuronal ensembles *in vivo,* in mouse dorsal DG following contextual fear conditioning (CFC). Labeled cells were mostly located in the granule cell layer (Figure 1C), suggesting that they are mostly dentate granule cells (DGCs). Both reporters showed low activation in the home cage (HC) condition, were robustly activated by kainic acid-induced seizures, and were mostly inhibited in the presence of Dox. Consistent with previous reports (Deng et al., 2013;

Lacagnina et al., 2019; Nakayama et al., 2015), on average 1–2% of the DGCs were labeled after CFC (Figure 1C). Both reporters also labeled small populations of cells, mostly mossy cells, in the dentate hilus regions. The number of labeled hilar cells was similar in the HC and CFC conditions, suggesting that contextual fear learning didn't significantly activate these reporters in the hilus (Figures S1E–S1I).

We next verified that activation of *F*-RAM and *N*-RAM *in vivo* specifically required *Fos* and *Npas4*, respectively. In *Fos* and *Npas4* conditional knockout mice ($Fos^{flx/flx}$ and $Npas4^{flx/flx}$), we deleted the *Fos* and *Npas4* gene, respectively, in DG using AAVs expressing the DNA recombinase Cre (Figures S1J and S1K). Seizure-induced *F*-RAM activity was largely abolished in the absence of *Fos*, but not after removal of *Npas4* (Figure 1D). The remaining activity of *F*-RAM may be due to the recruitment of other FOS/JUN family members such as c-JUN and FOSB, which may also bind and activate P_F-RAM (Hess et al., 2004). *Npas4* deletion, but not *Fos* deletion, eliminated *N*-RAM activity. Taken together, these results indicate that the *F*-RAM and *N*-RAM reporters specifically label the *Fos*- and *Npas4*-dependent active neuronal ensembles.

The *F*-RAM and *N*-RAM Reporters Define Distinct Neuronal Ensembles Within the Memory Engram

To determine whether the neuronal ensembles identified by *F*-RAM and *N*-RAM are distinct populations within the DG engram, we first examined synaptic properties of DGCs in each ensemble. Whole-cell patch-clamp recordings were carried out on *F*-RAM$^+$ or *N*-RAM$^+$ cells 24 hours after CFC (Figure 2A), measuring spontaneous miniature excitatory and inhibitory postsynaptic currents (mEPSCs and mIPSCs). Compared to their unlabeled (*F*-RAM$^-$ or *N*-RAM$^-$) neighbors, *F*-RAM$^+$ neurons received stronger excitatory inputs, specifically higher mEPSC frequencies (Figure 2B), while *N*-RAM$^+$ neurons received stronger inhibitory inputs, specifically increased mIPSC frequencies (Figure 2C). mIPSCs of *F*-RAM$^+$ neurons and mEPSCs of *N*-RAM$^+$ neurons were indistinguishable from those of their unlabeled neighbors. *F*-RAM$^+$ and *N*-RAM$^+$ neurons were rarely seen in the inner granule cell layer and did not show the high intrinsic excitability typical of adult new-born DGCs (Kuhn et al., 1996; Mongiat et al., 2009) (Figures S2A–S2C), suggesting that they are mature granule cells. Together, these data indicate that the *F*-RAM and *N*-RAM ensembles are mostly composed of mature granule cells with distinct synaptic properties.

We next measured co-localization of each ensemble and the *Fos*-expressing neurons that have been postulated to be engram cells (Garner et al., 2012; Tanaka et al., 2014; Tonegawa et al., 2015). We used the FosTRAP mouse (Guenthner et al., 2013), in which the endogenous *Fos* promoter drives the expression of Cre^{ER} to label *Fos*-expressing cells in green via a Cre-dependent EYFP reporter (Figure 2D). The *F*-RAM or *N*-RAM ensemble was simultaneously labeled red with mKate2 (Figure 2E). The *F*-RAM and Fos-Cre^{ER} ensembles, both of which should reflect *Fos* expression, showed substantial co-localization (49.902 ± 5.053%; Figure 2F); the incomplete overlap could be due to incomplete viral co-infection, different reporter temporal control (Dox-Off vs. Cre^{ER}) and different activity promoters (see Discussion). In addition, DGCs labeled by either *F*-RAM or Fos-Cre^{ER} alone, or both, all had similar electrophysiological properties: increased mEPSC frequencies

compared to unlabeled neurons (Figure S2D). In contrast, the *N*-RAM and Fos-Cre^{ER} ensembles showed little overlap (5.756 ± 2.522%; Figure 2F) and were electrophysiologically distinct: DGCs labeled by *N*-RAM, including the small population labeled by both *N*-RAM and Fos-Cre^{ER}, had higher mIPSC frequencies than unlabeled DGCs and those labeled only by Fos-Cre^{ER} (Figure S2E). These data further indicate that the *F*-RAM and *N*-RAM reporters likely capture distinct neuronal populations.

The *F*-RAM and *N*-RAM Ensembles Display Distinct Activity Patterns During Memory Recall

The distinct synaptic properties of the *F*-RAM and *N*-RAM ensembles suggest different roles in memory expression. We therefore investigated their functions in contextual fear memory discrimination-generalization, which is known to be mediated by the DG (Danielson et al., 2017; Guo et al., 2018; Knierim and Neunuebel, 2016; Senzai and Buzsaki, 2017). In an adopted memory discrimination-generalization assay (Huckleberry et al., 2016; Rozeske et al., 2018), mice were fear conditioned in context A, and exposed 24 hours later to either the conditioned context A, an unconditioned context B very similar to A, or a highly distinct context C (Figures 3A and S3B). Strong fear responses (freezing) were observed in the conditioned context A (Figure 3B). Clear fear responses were also observed in context B, suggesting a degree of memory generalization due to the similarity of the two contexts. Memory discrimination also occurred, however, as freezing levels in context B were significantly lower than in A. In context C mice displayed the basal level of freezing expected for a novel context, indicating strong memory discrimination and minimal generalization.

To understand the roles of the *F*-RAM and *N*-RAM ensembles, we first examined their reactivation during memory recall in the different contexts using expression of the IEG ARC (Figures 3C and 3D). The total numbers of ARC^{+} cells were similar in contexts A, B and C (Table S1), suggesting that all three contexts triggered similar levels of overall activity in the DG. The *F*-RAM ensemble showed similar rates of reactivation in contexts A and B but less in context C (Figure 3E), suggesting that the activity of *F*-RAM^{+} neurons is not sensitive to small differences between contexts and thus favors memory generalization. *N*-RAM^{+} neurons, however, were differentially reactivated, significantly less in context A than in B (Figure 3F). The greater reactivation of *N*-RAM^{+} neurons in context B was not an effect of novelty, because a lower rate of reactivation was observed in the novel context C. These results suggested that *N*-RAM^{+} neurons might be involved in mediating differential memory expression in similar contexts. Similar results were obtained using FOS instead of ARC as the activity marker (Figures S3C).

To confirm that the *F*-RAM and *N*-RAM ensembles were reactivated differently *in vivo*, we measured their calcium (Ca^{2+}) activity during memory recall using fiber photometry (Figure 3G). GCaMP6f, a genetically encoded Ca^{2+} indicator, was expressed in *F*-RAM^{+} or *N*-RAM^{+} neurons after CFC (Figure 3H) and GCaMP6f signals were measured when animals recalled memories in the three contexts in random order. Consistent with the IEG staining, the *F*-RAM ensemble showed similar strong Ca^{2+} activity during recall in contexts A and B, as quantified by the average Ca^{2+} signal (ΔF/F) over the entire recall session (Figures 3I and

3J). The *N*-RAM ensemble showed significantly less Ca^{2+} activity in context A than in B (Figures 3I and 3K). Remarkably, the difference in Ca^{2+} activity levels between contexts A and B ($\Delta F/F_{[(B-A)/(A+B)]}$) of the *N*-RAM (but not the *F*-RAM) ensemble was significantly correlated with the performance of an animal in discriminating between these two contexts ($Freezing_{[(A-B)/(A+B)]}$, Figure 3K), indicating that the *N*-RAM ensemble is important for memory discrimination.

The *F*-RAM and *N*-RAM Ensembles Differentially Regulate the Memory Discrimination-Generalization Balance

The previous results suggest that the *F*-RAM ensemble promotes memory generalization and the *N*-RAM ensemble mediates memory discrimination. To test this hypothesis, we chemogenetically manipulated the activity of *F*-RAM^+ and *N*-RAM^+ neurons during memory recall. By expressing the inhibitory (hM4Di) or excitatory (hM3Dq) DREADDs (Designer Receptors Exclusively Activated by Designer Drugs) (Roth, 2016) in the ensemble neurons (Figures 4A and 4B), we were able to inhibit or activate their activity with the DREADD agonist clozapine *N*-oxide (CNO), delivered by intraperitoneal (i.p.) injection 30 minutes before memory recall (Figures 4C and S4A). In addition to freezing levels in different contexts, discrimination indices (DIs) for context A vs. B and A vs. C were measured to detect bi-directional shifts in the discrimination-generalization balance.

Inhibiting the *F*-RAM ensemble enhanced discrimination between contexts A and B (Figures 4D and 4E), while inhibiting the *N*-RAM ensemble reduced memory discrimination (Figure 4F). These results suggest that the *F*-RAM and *N*-RAM ensembles shift the discrimination-generalization balance in opposite directions. Notably, these manipulations only affected discrimination between similar contexts (A and B), but not distinct contexts (A and C), consistent with the DG being involved primarily in distinguishing similar patterns (Bernier et al., 2017; Kheirbek et al., 2013; Treves and Rolls, 1994). These behavioral effects were not due to any non-specific effects of CNO (Figure S4C) or altered general locomotion or anxiety levels, as freezing levels in context C were similar across all treatments. Inhibiting the *F*-RAM or *N*-RAM ensembles labeled under the home cage condition did not affect memory discrimination-generalization either (Figures S4D–S4F). Activation of the *F*-RAM ensemble by hM3Dq enhanced memory generalization and diminished discrimination between contexts (Figure 4G), consistent with the idea that this ensemble promotes memory generalization. Activation of the *N*-RAM ensemble, however, did not affect discrimination (Figure 4H), suggesting that it is required for, but does not actively drive, memory discrimination.

Taken together, our results so far indicate that the contextual fear memory engram consists of functionally distinct neuronal ensembles, and those labeled by *F*-RAM and *N*-RAM oppositely modulate the balance between memory discrimination and generalization.

The *F*-RAM Ensemble Receives Increased Excitatory Inputs from the MEC, while the Ensemble Receives Enhanced Inhibitory Inputs from CCK^+ Interneurons

For two ensembles within the same engram to differentially modulate memory expression, we hypothesized that each ensemble would undergo different circuit modifications necessary

for their distinct functions. Since *F*-RAM$^+$ DGCs receive stronger excitatory inputs than their neighbors (Figure 2B), we asked which of the three major afferent pathways of the DG provide this increased excitatory drive: the lateral perforant path (LPP) from the lateral entorhinal cortex (LEC), the medial perforant path (MPP) from the medial entorhinal cortex (MEC) or the mossy cell fibers (MCF) from the dentate hilus (Amaral and Witter, 1989) (Figure 5A). We electrically stimulated the axonal fibers of the LPP, MPP or MCF, which respectively target the outer, middle or inner molecular layers (OML, MML, IML) of the DG (Scharfman and Myers, 2013; Witter, 2007), and simultaneously measured evoked excitatory postsynaptic currents (eEPSCs) of *F*-RAM$^+$ and unlabeled neighboring neurons in pairs. Selective stimulation of the input pathways was confirmed by observation of their characteristic short-term plasticity: paired-pulse facilitation for the LPP and MCF and paired-pulse depression for the MPP (Hashimotodani et al., 2017; Petersen et al., 2013), and by selective reduction of the MPP response in the presence of the mGluR2/3 agonist DCG-IV (Macek et al., 1996) (Figure 5B). The amplitude of eEPSCs originating from the MPP only was significantly larger on *F*-RAM$^+$ than *F*-RAM$^-$ cells (Figure 5C). In contrast, eEPSCs from all three pathways were similar in *N*-RAM$^+$ neurons and their unlabeled neighbors (Figure 5F). Paired-pulse ratios (PPRs) and AMPA/NMDA ratios were comparable in *F*-RAM$^+$ and *F*-RAM$^-$ neurons (Figures 5D and 5E). These findings were confirmed using optogenetic stimulation (Figure S5C). Therefore, inputs to *F*-RAM$^+$ neurons from the MEC, but not the LEC or dentate hilus, were selectively strengthened.

To identify the source of the inhibitory inputs recruited onto *N*-RAM$^+$ DGCs (Figure 2C), we expressed light-activated channelrhodopsin (ChR2) in DG GABAergic neurons, by delivering AAV-EF1α-DIO-ChR2-EYFP into Gad2-Cre mice (Figures 5G and 5H). Optically evoked inhibitory postsynaptic currents (oIPSCs) were then measured on *N*-RAM$^+$ or *F*-RAM$^+$ DGCs and their unlabeled neighbors (Figure 5I). Consistent with our previous finding that *N*-RAM$^+$ neurons had higher mIPSC frequencies, robustly larger oIPSC amplitudes were observed on *N*-RAM$^+$ cells, with PPRs being similar in *N*-RAM$^+$ and *N*-RAM$^-$ cells (Figure 5J). In contrast, oIPSCs on *F*-RAM$^+$ neurons were similar to those of their unlabeled neighbors (Figure S5E).

The three major subtypes of GABAergic interneuron in DG are parvalbumin- (PV$^+$), somatostatin- (SST$^+$) and cholecystokinin-expressing (CCK$^+$) cells (Freund and Buzsaki, 1996; Pelkey et al., 2017). To determine whether inputs from certain of these interneuron subtypes were recruited to *N*-RAM$^+$ DGCs, oIPSCs were measured on pairs of *N*-RAM$^+$ and *N*-RAM$^-$ cells in the presence of the P/Q-type Ca^{2+} channel blocker ω-agatoxin IVa (AgTx), to selectively inhibits transmission from PV$^+$ interneurons, or the N-type Ca^{2+} channel antagonist ω-conotoxin GVIa (CnTx), to selectively inhibits transmission from CCK$^+$ interneurons (Hefft and Jonas, 2005) (Figure 5K). The difference in oIPSC amplitudes between *N*-RAM$^+$ and *N*-RAM$^-$ neurons was abolished in the presence of CnTx, but not AgTx (Figure 5L), suggesting that the increased inhibition on *N*-RAM$^+$ neurons comes mainly from CCK$^+$ interneurons. Consistently, the increase in oIPSC amplitudes on *N*-RAM$^+$ neurons was also abolished by the CB_1R agonist WIN 55,212–2 (WIN), which selectively inhibits CCK$^+$ interneurons via the endocannabinoid pathway (Tsou et al., 1999). These results suggest that *N*-RAM$^+$ neurons recruit enhanced inhibitory drive selectively from CCK$^+$ interneurons.

The Distinct Synaptic Properties of Ensemble Neurons are Induced by Learning

Are the distinct synaptic properties of *F*-RAM$^+$ and *N*-RAM$^+$ neurons intrinsic features of the cells or acquired through learning? We hypothesized that these features were triggered by contextual fear learning via activation of the *Fos*- and *Npas4*-dependent pathways. We first determined whether these synaptic properties can be induced by the expression of *Fos* or *Npas4*. We artificially induced *Fos* and *Npas4* expression (FOS_{ind} and $NPAS4_{ind}$) in sparse and randomly selected DGCs (Figures 6A and 6B), and compared mEPSCs and mIPSCs on those neurons to their un-manipulated neighbors. *Fos* expression led to an increase in mEPSC frequencies (Figure 6C), recapitulating this synaptic feature of *F*-RAM$^+$ neurons. *Npas4* expression resulted in elevated mIPSC frequencies (Figure 6D), mimicking the synaptic changes observed on *N*-RAM$^+$ cells. Neither mIPSCs of FOS_{ind} neurons nor mEPSCs of $NPAS4_{ind}$ neurons were altered (Figures S6A and S6B). These results suggest that activation of *Fos*- and *Npas4*-dependent pathways may be sufficient to induce the synaptic properties observed in *F*-RAM$^+$ and *N*-RAM$^+$ neurons, respectively.

Since *Fos* and *Npas4* expressions are very low at baseline and highly activated by learning (Ramamoorthi et al., 2011), we predicted that the synaptic properties of the ensemble neurons are not pre-existing, but rather are induced by learning. Like all activity reporters, *F*-RAM and *N*-RAM can only identify ensembles after learning, so we cannot compare ensemble neurons before and after CFC. However, if the synaptic properties of interest are indeed induced by learning, we would expect that a stronger learning experience, resulting in a stronger memory, will induce stronger synaptic modifications (Choi et al., 2018). We therefore trained mice in a novel context with no foot shocks, weak foot shocks (0.35 mA) or strong foot shocks (0.55 mA; as used for other experiments) (Figure 6E). These 3 treatments resulted in correspondingly different strengths of contextual fear memory, as the animals displayed freezing levels that were closely correlated with the intensity of shocks they received (Figure 6F). The numbers of labeled *F*-RAM$^+$ and *N*-RAM$^+$ neurons were similar in the three groups (Figures S6C and S6D). Measuring oEPSCs from the MEC onto paired *F*-RAM$^+$ and *F*-RAM$^-$ DGCs and oIPSCs from CCK$^+$ interneurons onto paired *N*-RAM$^+$ and *N*-RAM$^-$ DGCs, we found that MEC input to *F*-RAM$^+$ and CCK inhibition on *N*-RAM$^+$ cells were strongest in mice that received strong foot shocks, followed by animals that received weak foot shocks and then those that received no foot shocks (Figures 6G–6L; CCK$^+$ interneurons were labeled using a genetic intersection strategy described in Figure 7I). These results, together with our previous data, suggest that the distinct synaptic properties of the ensemble neurons are the result of learning-induced synaptic modifications driven by distinct activity-dependent pathways.

The MEC and its Inputs to the DG Mediate Memory Generalization while DG CCK$^+$ Interneurons Mediate Memory Discrimination

These learning-induced circuit modifications in the *F*-RAM and *N*-RAM ensembles suggest important roles for the MEC and DG CCK$^+$ interneurons in memory discrimination-generalization. We first determined whether the MEC, like the *F*-RAM ensemble, promotes memory generalization. MEC activity was inhibited during memory recall by virally delivering hM4Di to MEC projection neurons, precisely and strongly targeting their axonal projections in the MML (Figure 7A). CNO injection then robustly suppressed, although did

not completely abolish, the activity of MEC neurons (Figure S7C). In the same memory discrimination-generalization assay described above (Figure 7B), inhibiting the MEC in this way suppressed memory generalization and enhanced discrimination between contexts A and B (Figure 7C), recapitulating the effect of inhibiting the *F*-RAM ensemble. Inhibiting the LEC in the same way did not affect memory generalization (Figures 7A and 7D).

To confirm that the MEC-DG pathway promotes memory generalization, we optogenetically inhibited MEC terminals within the DG (Figures 7E and 7F). Illuminating the DG with 561 nm light in animals expressing the inhibitory opsin eNpHR3.0 in the MEC significantly reduced the number of FOS^+ cells in the DG, but not in the nearby CA1 region that also receives MEC inputs, indicating selective inhibition of the MEC-DG pathway (Figure S7E). Inhibiting the MEC-DG projections in this way enhanced discrimination between contexts A and B (Figures 7G and 7H), similar to inhibition of the *F*-RAM ensemble. In control experiments without light stimulation mice injected with NpHR were indistinguishable from those injected with EYFP (Figure S7G). These results reveal an important role for the MEC-DG pathway in mediating memory generalization, likely involving the *F*-RAM^+ ensemble neurons.

We next examined the role of CCK^+ interneurons in mediating memory discrimination, by chemogenetically inhibiting DG CCK^+ interneurons during memory recall. CCK is expressed in both GABAergic and some glutamatergic neurons (Taniguchi et al., 2011), so we adopted a genetic intersection strategy to label only the GABAergic CCK^+ cells: using AAV-Dlx5/6-DIO-hM4Di-mCherry to drive Cre-dependent expression of hM4Di from an interneuron-specific promoter, Dlx5/6 (Dimidschstein et al., 2016), in CCK-Cre mice (Figure 7I). The majority of labeled neurons were $GAD67^+$, indicating successful intersectional labeling (Figures 7J and 7K). Labeled neurons displayed electrophysiological properties reported for CCK^+ interneurons, namely adaptive firing, depolarization-induced suppression of inhibition (DSI) and asynchronous synaptic transmission (Bartos and Elgueta, 2012) (Figures S7H–S7M). Using the same behavioral assay (Figure 7L), we then found that inhibiting DG CCK^+ interneurons abolished discrimination between contexts A and B and also significantly reduced discrimination between A and C (Figure 7M). In contrast, inhibiting PV^+ or SST^+ interneurons in the DG did not affect memory discrimination (Figures 7N and 7O). These results suggest that DG CCK^+ interneurons are involved in memory discrimination.

Discussion

Here we provide direct experimental evidence for functional heterogeneity within memory engrams. We show that two distinct neuronal ensembles (*F*-RAM and *N*-RAM) in representations of the same memory exhibit different synaptic properties and promote opposing behavioral outputs: memory generalization and memory discrimination. In addition, we describe synaptic mechanisms underlying this functional heterogeneity: the *F*-RAM and *N*-RAM ensembles selectively recruit excitatory and inhibitory inputs, respectively, from different upstream circuits. We show that these circuits regulate the discrimination-generalization balance: the MEC is important for memory generalization and DG CCK^+ interneurons for memory discrimination. While the present study focuses on

contextual fear conditioning in the DG, heterogeneity of the engram could be a widespread phenomenon (Grewe et al., 2017; Jun et al., 2010; Mallory and Giocomo, 2018): memory engrams may generally be composed of multiple functional subcomponents that differentially modulate experience-dependent behavioral outputs.

How Should We Genetically Define Functionally Distinct Neuronal Ensembles?

Critical questions remain regarding how many distinct ensembles there are and how best to define them genetically. Our findings suggest that the emergence of distinct subpopulations within memory engrams can result from different activity-dependent signaling cascades, triggered within individual ensembles by learning (Figure 6). Neuronal activity-dependent pathways are therefore key molecular mechanisms determining the functions of these ensembles, as well as providing activity markers to define them. Here we have investigated ensembles associated with two pathways, but other activity-dependent pathways such as *Arc* and *CREB* may define additional functionally distinct subpopulations (Denny et al., 2014; Park et al., 2016). Many of these pathways have overlapping upstream signaling and may be co-activated in some neurons (Lonergan et al., 2010). Although multiple lines of evidence from our study indicate that the *F*-RAM and *N*-RAM ensembles in DG are distinct neuronal populations (Figures 2–4), our data do not exclude the possibility of some overlap. A challenge for the future is to identify sets of orthogonal activity-dependent reporters that define distinct populations and provide a complete description of the memory engram.

Unlike most activity reporters, *F*-RAM and *N*-RAM report IEG-dependent downstream transcriptional output rather than expression of IEGs themselves. It is conceivable that the *F*-RAM and *N*-RAM ensembles are not identical to those defined by the native *Fos* and *Npas4* promoters, which may help to explain the incomplete overlap of the *F*-RAM and Fos-CreER ensembles (Figure 2F). Since transcription factors exert their functions through their downstream transcriptional targets, reporters such as *F*-RAM and *N*-RAM that monitor transcriptional outputs may better capture functional populations that undergo learning-induced changes.

It is also not known how neurons are recruited from the general population into the kinds of functionally distinct ensembles we describe here. Factors including intrinsic excitability (Yiu et al., 2014; Zhou et al., 2009), connectivity (Ryan et al., 2015) and firing patterns (Tanaka et al., 2018) have been suggested. Future work, for example using time-lapse Ca^{2+} imaging and single-cell sequencing, will determine whether extrinsic or intrinsic factors or a mixture of both contribute to the formation of functionally distinct neuronal ensembles.

What Information is Encoded in the *F*-RAM and *N*-RAM Ensembles?

Intriguingly, neither the *F*-RAM nor *N*-RAM ensemble is required for memory retrieval in the conditioned context (Figure 4), and neither is the DG *Fos*-expressing ensemble (Figures S4G–S4K) (Pignatelli et al., 2018). These results are not unexpected given that lesion or optogenetic inhibition of the entire DG does not impair memory retrieval (Kheirbek et al., 2013; Lee and Kesner, 2004), although inhibiting the DG *Arc*-expressing ensemble reduced freezing (Denny et al., 2014). The *F*-RAM and *N*-RAM ensembles therefore resemble the postulated “higher-order memory trace” (Thompson, 2005). Unlike the “essential memory

trace", the "higher-order memory trace" is not absolutely required for memory retrieval, but is involved in modulating memory-guided adaptive behaviors. Future work that combines *in vivo* imaging with functional perturbation to decipher the specific information encoded by each ensemble is urgently needed to test and revise current models of memory.

Learning-induced Synaptic Changes in Neuronal Ensembles

The synaptic properties of *F*-RAM$^+$ and *N*-RAM$^+$ neurons (Figures 2A–2C) are most likely the result of neuronal activity triggered during contextual fear learning, because they correlate with memory strength and can be induced by the expression of FOS and NPAS4, respectively (Figure 6). However, since the ensembles can only be labeled after they have been activated, we cannot exclude the possibility that other differences between these two groups of neurons already exist prior to the experience.

In addition to the potentiation of excitatory inputs, which has been the primary focus of work on mechanisms of memory encoding, our data suggest that the potentiation of inhibitory inputs is also important. Furthermore, strengthening of excitatory and inhibitory inputs occurs on two different neuronal ensembles within the memory engram, which could provide a mechanism for a neural system to balance the behavioral output (e.g., discrimination vs. generalization) through the "push and pull" of different neuronal ensembles. It remains to be seen whether the *F*-RAM and *N*-RAM ensembles interact with each other.

Circuit Components Involved in the Discrimination-Generalization Balance

Mossy cells.—Both *F*-RAM and *N*-RAM reporters label small numbers of hilar mossy cells (1–6%), which have recently been implicated in pattern separation (Danielson et al., 2017; GoodSmith et al., 2017; Jinde et al., 2012; Senzai and Buzsaki, 2017). However, the numbers of mossy cells labeled by either reporter were similar between the HC and CFC conditions (Figures S1E and S1F). Although other explanations are possible, given that animals were treated identically throughout the 2–3 day window for reporter labeling (Figure 1C) except for the few minutes during which one group received CFC treatment, it is likely that the reporters captured mossy cells that were active in the home cage and CFC did not activate additional mossy cells. Furthermore, memory discrimination-generalization was not affected when the mossy cells labeled in the HC condition were inhibited (Figures S4D–S4F). These results suggest that the *F*-RAM and *N*-RAM reporters do not capture the mossy cell CFC engram. Genetic tools that can specifically label mossy cells activated during contextual learning will be needed to define the role of mossy cells in memory discrimination-generalization.

MEC.—Our data strongly support a role for the MEC-DG pathway in memory generalization, in line with observations that grid cells in the MEC maintain relatively stable spatial firing patterns across similar contexts (Fyhn et al., 2007; Leutgeb et al., 2007). In our study, memory retrieval (in context A) was not impaired by suppressing MEC activity (Figure 7C). This observation is consistent with some published studies (Hales et al., 2014; Kanter et al., 2017) but contradictory to others (Kitamura et al., 2015; Miao et al., 2015; Zhao et al., 2016). The discrepancy may be explained by the different MEC cell populations

being targeted and the different manner in which they are being inhibited (lesion, optogenetics, chemogenetics). Future work is needed to pinpoint which MEC subpopulations (Diehl et al., 2017) relay generalization signals to the DG.

CCK$^+$ interneurons.—Of the three major subtypes of interneurons providing inhibitory inputs to DG granule cells, we find that CCK$^+$ and not PV$^+$ or SST$^+$ interneurons are important for memory discrimination. The reason for this is not known. In fact, the roles of CCK$^+$ interneurons in learning and memory have not been extensively studied. CCK$^+$ interneurons are known to have unique synaptic outputs, such as endocannabinoid-dependent short-term and long-term synaptic plasticity (Castillo et al., 2012; Hartzell et al., 2018) and asynchronous synaptic release (Hefft and Jonas, 2005). Our results present an exciting opportunity to identify specific synaptic mechanisms uniquely provided by CCK$^+$ interneurons to regulate memory discrimination.

STAR METHODS

LEAD CONTACT AND MATERIALS AVAILABILITY

Further information and requests for reagents may be directed to and will be fulfilled by the lead contact, Dr. Yingxi Lin (yingxi@mit.edu or linyi@upstate.edu).

The *F*-RAM and *N*-RAM reporters generated in this study have been deposited to Addgene (ID: 140274 and 140275). All other unique reagents generated in this study are available from the Lead Contact with a completed Materials Transfer Agreement.

EXPERIMENTAL MODEL AND SUBJECT DETAILS

Subjects—7–11 week old C57BL/6 male and female mice were used for all experiments. Wildtype mice were purchased from the Charles River Laboratory. *Npas4*$^{flx/flx}$ (*Npas4* conditional knockout) mice were generated previously (Lin et al., 2008) and *Fos*$^{flx/flx}$ (*Fos* conditional knockout) mice were generously provided by Dr. Ming Xu at the University of Chicago. Gad2-Cre (*Gad2*$^{tm2(cre)Zjh}$/J), CCK-Cre (*Cck*$^{tm1.1(cre)Zjh}$/J), PV-Cre (*Pvalb*$^{tm1(cre)Arbr}$/J), SST-Cre (*Sst*$^{tm2.1(cre)Zjh}$/J) and Fos-Cre^{ER} (*Fos*$^{tm1.1(cre/ERT2)Luo}$/J) mice were purchased from the Jackson Laboratory. To produce Cre-expressing animals, heterozygous or homozygous mice carrying the Cre allele were bred with wildtype animals from the Charles River Laboratory. All mice were housed with a 12 hour light-dark cycle. Animal protocols were performed in accordance with NIH guidelines and approved by the Massachusetts Institute of Technology Committees on Animal Care and the Institutional Animal Care and Use Committee at SUNY Upstate Medical University.

METHOD DETAILS

Cell cultures for luciferase assays—Primary hippocampal neurons were prepared from mouse pups at postnatal day 0 as previously described (Ramamoorthi et al., 2011) and plated at 100,000 cells per well on coated 24-well plates. Cultures were kept in dissection medium [Neurobasal A Medium (NBA, Invitrogen), 10% horse serum (Invitrogen) and GlutaMAX (Invitrogen)] for 3 hours before being switched to culture medium [NBA

supplemented B27 (Invitrogen) and GlutaMAX]. Cultures were kept at 37 °C in humidified incubators supplemented with 5% CO_2 until use.

At 5 days *in vitro* (DIV), neurons were transfected with plasmids using lipofectamine 2000 (Life Technologies). Plasmid cocktails contained: luciferase reporter plasmids ($P_{F\text{-RAM}}$-Luc or P_{N}-RAM-Luc) expressing firefly luciferase under the control of $P_{F\text{-RAM}}$ or $P_{N\text{-RAM}}$, control plasmids (TK-Renilla) expressing renilla luciferase under the control of the constitutively active thymidine kinase promoter (Promega) and plasmids that overexpress *Fos* or *Npas4* under the control of a constitutive promoter (EF1α) in some cases.

At 8 DIV, cultures were blocked with tetrodotoxin (TTX, 1 μM, Tocris) and APV (100 μM, Tocris) for 1 hour prior to stimulation and then stimulated for 6 hours with 34 mM KCl or 34 mM KCl plus 5 mM EGTA (Sigma). Normal culture medium without a high concentration of KCl was used to treat the unstimulated control group. Neurotrophic factors and other drugs were directly added to the cultures in 10 μL culture medium and the neurons were incubated for 6 hours. At the end of the experiment, neurons were rinsed briefly in phosphate buffered saline (PBS, Invitrogen) and lysed in passive lysis buffer (Promega) for 20 minutes at room temperature. Dual-Glo Luciferase Assay System (Promega) reagents were used to measure luciferase levels using the SpectraMax Microplate Reader (Molecular Devices). For each experiment, relative luciferase values (a.u.) were calculated by normalizing the firefly luciferase level to the renilla luciferase level. Data were compiled from 3 separate batches of cultures, each conducted with 2 to 3 replicates.

Neurotrophic factors and other drugs were dissolved in water and used at the following final concentrations: recombinant human BDNF (50 ng/μL, PeproTech), recombinant human NT3 (50 ng/μL, PeproTech), recombinant human NT4 (50 ng/μL, PeproTech), NKH 477 (20 μM, Tocris), Bicuculline (50 μM, Sigma) and 4-aminopyridine (250 μM, Tocris).

Viral vectors—AAV1-hSyn-GFP, AAV1-hSyn-GFP-Cre, AAV1-EF1α-DIO-ChR2-EYFP were obtained from the University of Pennsylvania Vector Core via Addgene. All other AAVs were produced in house. AAVs were generated in HEK293T cells and purified using an adapted h gradient purification protocol as previously described (Sørensen et al., 2016). Viral dilutions were determined for individual experiments using pilot injections.

In experiments to label the *F*-RAM and *N*-RAM ensembles *in vitro* and *in vivo*, AAV2/AAV8-*F*-RAM-d2tTA-TRE-mKate2 or AAV2/AAV8-*N*-RAM-d2tTA-TRE-mKate2 virus was used. AAV2/AAV8s were mixtures of AAV2/2 (rep/cap) and AAV2/8 serotypes at a 1:1 ratio (Sørensen et al., 2016). In most experiments a control virus (AAV2/AAV8-EF1α-EGFP) was co-injected to determine injection accuracy and infection efficiency. To determine whether the *F*-RAM and *N*-RAM reporters were dependent on endogenous *Fos* and *Npas4*, AAV9-*F*-RAM-d2tTA-TRE-mKate2 or AAV9-*N*-RAM-d2tTA-TRE-mKate2 virus was co-injected with AAV1-hSyn-GFP or AAV1-hSyn-GFP-Cre into *Npas4* or *Fos* conditional knockout mice. To examine co-localization of the Fos-Cre^{ER} ensemble and either the *F*-RAM or *N*-RAM ensemble, AAV9-*F*-RAM-d2tTA-TRE-mKate2 or AAV9-*N*-RAM-d2tTA-TRE-mKate2 virus was co-injected with a Cre-dependent reporter virus, AAV1-EF1α-DIO-ChR2-EYFP. For the fiber photometry experiments, viral cocktails

containing AAV9-TRE-GCaMP6f and either AAV9-*F*-RAM-d2tTA-TRE-mKate2 or AAV9-*N*-RAM-d2tTA-TRE-mKate2 were used.

To manipulate ensemble activity with DREADDs, viral cocktails containing AAV9-TRE-hM3Dq-mCherry or AAV9-TRE-hM4Di-mCherry and either AAV9-*F*-RAM-d2tTA-sEF1α-GFP or AAV9-*N*-RAM-d2tTA-sEF1α-GFP were used (the sEF1α-GFP component was used to determine injection accuracy and infection efficiency). For control experiments testing the effects of CNO injections alone, AAV9-TRE-mCherry was used instead of the DREADD-expressing viruses and was co-injected with AAV9-*N*-RAM-d2tTA-sEF1α-GFP. In experiments to manipulate the activity of *Fos*-expressing ensembles, AAV9-pFos-d2tTA was co-injected with the DREADD viruses. pFos is an engineered *Fos* promoter similar to that used in previous studies (Liu et al., 2012; Reijmers et al., 2007).

To examine optically evoked IPSCs (oIPSCs) from DG interneurons, AAV2/AAV8-*F*-RAM-d2tTA-TRE-mKate2 or AAV2/AAV8-*N*-RAM-d2tTA-TRE-mKate2 virus was co-injected with AAV2/AAV8-EF1α-DIO-ChR2-EYFP virus into Gad2-Cre mice. To examine oIPSCs from DG CCK^+ interneurons, AAV9-*F*-RAM-d2tTA-TRE-mKate2 or AAV9-*N*-RAM-d2tTA-TRE-mKate2 virus was co-injected with AAV9-Dlx5/6-DIO-ChR2-EYFP virus into CCK-Cre mice. To examine optically evoked EPSCs (oEPSCs) that originate from the medial entorhinal cortex (MEC) and the lateral entorhinal cortex (LEC), AAV9-EF1α-DIO-ChR2-EYFP and AAV1-CaMKII-Cre-GFP were co-injected into these regions and AAV9-*F*-RAM-d2tTA-TRE-mKate2 was injected into the DG. To examine oEPSCs that originate from the dentate hilus, AAV9-EF1α-DIO-ChR2-EYFP and AAV1-CaMKII-Cre-GFP were co-injected into the contralateral DG and AAV9-*F*-RAM-d2tTA-TRE-mKate2 was injected into the ipsilateral DG, where whole-cell patch-clamp recordings were carried out.

To over-express FOS or NPAS4 in sparse populations of DG neurons, animals were injected with the following viral cocktail: AAV9-CAG-tTA, AAV1-TRE-Cre (1:1,000 dilution), AAV9-hSyn-DIO-FOS/NPAS4, and AAV1-EF1α-DIO-EYFP.

In experiments to suppress the activity of MEC or LEC projection neurons, AAV1-CaMKII-Cre-GFP and AAV9-hSyn-DIO-hM4Di-mCherry were co-injected into the MEC or LEC. In experiments to optogenetically inhibit the MEC-DG pathway, AAV9-EF1α-DIO-eNpHR3.0-EYFP or AAV9-EF1α-DIO-EYFP was co-injected with AAV1-CaMKII-Cre-GFP into the MEC. To manipulate the activity of DG interneurons with DREADDs, AAV9-Dlx5/6-DIO-hM4Di-mCherry was injected into CCK-Cre, PV-Cre or SST-Cre mice.

Stereotaxic viral injection and fiber implantation—Mice were anesthetized with 1.5–2% isoflurane in O_2. To label and manipulate *F*-RAM and *N*-RAM ensembles in the DG, stereotaxic injections were performed bilaterally into the dorsal hippocampal DG with the following coordinates (relative to bregma) and volumes: AP −1.90 mm, ML ±1.30 mm, DV −2.00 mm, 150–200 nL per hemisphere. Viruses were infused at a rate of 100 nL per minute and needles were kept at the injection site for 5 minutes. The same coordinates and volumes were used to manipulate interneurons in the DG. To manipulate the activities of MEC and LEC projection neurons, the following coordinates and volumes were used: MEC (AP −4.75 mm, ML ±3.25 mm, DV −3.60 mm, 250–300 nL per hemisphere), LEC (AP

−3.40 mm, ML ±4.35 mm, DV −4.10 mm, 250–300 nL per hemisphere). Mice were typically allowed to recover for 6–8 days following surgery. For experiments with Dox-dependent ensemble labeling, animals were put on Dox diet (40 mg/kg, Bio-Serv) after surgery.

For fiber photometry experiments, DG injections were performed unilaterally, followed by fiber implantation in the same procedure. The left or right hemisphere was randomly chosen for unilateral surgeries. Fiber implants were made of multimode fiber (400 μm core, 0.48 NA, Thorlabs) with plastic ferrules (2.5 mm, Thorlabs). Implants were placed unilaterally in the DG 0.20 mm above the injection site (AP −1.90 mm, ML ±1.30 mm, DV −1.80 mm).

For optogenetics experiments, viral injections into the MEC were followed by fiber implantation in the DG. Fiber implants were made of multimode fiber (200 μm core, 0.22 NA, Thorlabs) with plastic ferrules (1.25 mm, Thorlabs). Implants were placed bilaterally in the DG (AP −1.90 mm, ML ±1.30 mm, DV −1.80 mm).

For DG injections, only animals with viral infection of more than 80% of the dorsal DG and less than 20% of CA3 were included in behavioral analyses. For MEC or LEC injections, only animals with selective infection of MEC or LEC axonal terminals in either the middle (MML) or outer (OML) third of the DG molecular layers were included. These histological analyses were performed by investigators blind to the genotypes or conditions.

Drug injections—To induce seizure, kainic acid (KA, Sigma) was dissolved in saline (1 mg/mL, Teleflex Medical) and injected i.p. at 18 mg/kg. Animals were sacrificed 1.5 hours later to check immediate early gene expression, or 24 hours later to check *F*-RAM and *N*-RAM expression.

In experiments using Fos-Cre^{ER} mice, tamoxifen (Sigma) was dissolved in corn oil (Sigma) overnight at 37 °C (15 mg/mL) and injected i.p at 150 mg/kg 24 hours prior to behavioral assays. Tamoxifen solution was stored at 4 °C for no more than 24 hours before use.

Clozapine *N*-oxide (CNO, Tocris) was dissolved in DMSO (Sigma) at 20 mM and stored at −20 °C. Before experiments, stock CNO was diluted in saline to the desired concentration, 0.4 mg/mL for hM4Di or 0.05 mg/mL for hM3Dq. The same amount of DMSO was diluted in saline as vehicle control. Fresh CNO was injected i.p. at 4 mg/kg for hM4Di or 0.5 mg/kg for hM3Dq 30 minutes before memory recall. CNO doses were determined by pilot experiments and are similar to published studies. For the control experiment testing the effects of CNO injection alone without DREADD expression, a 4 mg/kg dose was used. Diluted CNO solution was kept at 4 °C for up to 24 hours before use.

Contextual fear conditioning (CFC)—Prior to CFC, mice were handled daily in a holding room for 3 days. For experiments with Dox-dependent ensemble labeling, on the third handling day the Dox diet was replaced by regular diet (off Dox) after the last handling session. In control experiments testing reporter expression in the presence of Dox (CFC + Dox), animals were kept on Dox diet throughout. Behavioral assays were typically carried out 48 hours after the last handling session.

On the training day, mice were first transported into the holding room and allowed to acclimatize for at least 30 minutes, then transported into the behavioral room and placed in context A: 24 cm (L) × 19 cm (W) × 17.5 cm (H), with steel grid floors and 1% acetic acid (Sigma). Mice were conditioned as follows: animals were allowed to explore the conditioned chamber freely for 4 minutes and received 2 second 0.55 mA foot shocks at 1 minute intervals 3 times, starting at the 58th second. After each experiment, the chamber was cleaned with 70% ethanol and then with water. In experiments to examine whether synaptic features of ensemble neurons depend on memory strength, no foot shock, weak foot shocks (0.35 mA), or strong foot shocks (0.55 mA, the same as other CFC experiments) were delivered. For experiments with Dox-dependent ensemble labeling, animals were switched back to Dox diet 24 hours after CFC if subsequent behavioral experiments were needed.

To test contextual fear memory discrimination-generalization, 24–48 hours after CFC conditioned mice were returned to the same behavioral room and placed in the conditioned context (A), a similar context (B) or a distinct context (C) for memory recall for 4 minutes. Context B shares all features with context A except that a soft pad insert is used as the floor. Context C uses a different chamber that has white opaque walls, is 32 cm (L) × 25 cm (W) × 32 cm (H), has a soft padded floor, and is scented with 0.25% benzaldehyde (Sigma). In some of the experiments, animals were tested for memory recall in only one context, either A, B or C, and sacrificed 1.5 hours later for immunohistochemistry. In chemogenetics and fiber photometry experiments, the same animals were tested in multiple contexts in order to examine discrimination between contexts. In those cases, fear conditioned animals were tested in contexts B and A on the first day (with at least 6 hours in between), and contexts C and A on the following day.

Contextual fear memory expression was measured by manually scoring freezing behavior over the 4 minute recall period, sampling every 5 seconds, with freezing defined as absence of movement for at least 1 second. Discrimination indices (DIs) are calculated as $\text{Freezing}_{[(A-B)/(A+B)]}$ when comparing freezing levels in contexts A and B, or $\text{Freezing}_{[(A-C)/(A+C)]}$ when comparing freezing levels in contexts A and C. Scorers were blind to the experimental conditions. For example, for chemogenetics experiments researcher 1 would randomly assign CNO or Veh treatments to the animals and perform the drug injection; researcher 2 would carry out the behavioral testing and quantify the freezing behaviors without knowing the treatments.

Immunohistochemistry and confocal imaging—Animals were either perfused or drop fixed with 4% paraformaldehyde (PFA, Sigma) in PBS. For experiments examining IEG expression, animals were sacrificed 1.5 hours after the last behavioral test. Coronal sections were cut at 50 μm thickness. For typical immunohistochemistry experiments, brain slices were washed in PBS for 10 minutes 3 times and blocked for 2 hours at room temperature with blocking solution: 1% Triton X-100 (Sigma) and 10% goat serum (Invitrogen) in PBS. Slices were then incubated with primary antibody overnight at 4 °C in the antibody solution: 0.1% Triton X-100 and 5% goat serum in PBS. Next day slices were washed in PBS for 10 minutes 3 times and incubated with secondary antibody for 2 hours at room temperature in antibody solution. Finally, slices were washed in PBS for 10 minutes 3 times and mounted with DAPI Fluoromount-G (Southern Biotech). When staining GAD67,

a minimum-detergent protocol was adopted from a previous study (Dimidschstein et al., 2016): after initial washing with PBS following PFA fixation, brain slices were permeabilized with 0.1% Triton X-100 for 30 minutes. Slices were then blocked and stained in a detergent-free solution: 3% bovine serum albumin (Sigma) and 5% goat serum in PBS. In this case slices were incubated with anti-GAD67 primary antibody for 48 hours at room temperature.

Antibodies used and dilutions are as follows: rabbit anti-Npas4 (1:10,000, home-made), rabbit anti-Fos (1:1,000, Santa Cruz), rabbit anti-Fos (1:1,000, Synaptic Systems), guinea pig anti-Arc (1:1,000, Synaptic Systems), rabbit anti-mGluR2/3(1:500, Millipore), mouse IgG2a anti-GAD67 (1:500, Millipore) and Alexa 488, 555, 647 secondary antibodies (1:500, Invitrogen).

All images were acquired using an Olympus Fluoview FV1000 confocal microscope. For most cell counting experiments high-resolution z-stack images of the DG were acquired using either a 20× or a 60× oil-immersion objective. Numbers of positive cells were determined manually from 6–12 images per animal as previously described (Sørensen et al., 2016). Analyses were performed by investigators who were blind to the experimental conditions.

Electrophysiology—Mice were subjected to electrophysiology 24–48 hours after CFC. Mice were anesthetized and perfused with carbogenated (95% O_2, 5% CO_2) ice-cold cutting solution containing (in mM): 210 sucrose, 2.5 KCl, 1.24 NaH_2PO_4, 8 $MgCl_2$, 1 $CaCl_2$, 26 $NaHCO_3$, 20 Glucose and 1.3 sodium-L-ascorbate, ~340 mOsm osmolarity, pH 7.3. Brains were immediately dissected out. 300 μm transverse slices were cut using a vibratome (VT1200, Leica). Slices were transferred to warm (32 °C) carbogenated recovery solution, containing 50% cutting solution and 50% ACSF. ACSF contains (in mM): 119 NaCl, 2.5 KCl, 1.24 NaH_2PO_4, 1.3 $MgCl_2$, 2.5 $CaCl_2$, 26 $NaHCO_3$, and 10 glucose, 305 mOsm osmolarity, pH 7.3. Slices were recovered at 32 °C for 15 minutes, then transferred to another chamber filled with room temperature (~23 °C) ACSF. Slices were kept in ACSF for at least 30 minutes before recording.

All recordings were performed in a chamber perfused with carbogenated ACSF at room temperature at a flow rate of 2 mL/min. Whole-cell patch-clamp recordings were performed using borosilicate glass pipettes (3–6 MΩ tip resistance). mEPSCs were pharmacologically isolated with 0.5 μM tetrodotoxin (TTX, Tocris) and 50 μM picrotoxin (Tocris), and recorded from cells voltage clamped at −70 mV using Cs-based internal solution containing (in mM): 130 $CsMeSO_3$, 10 phosphocreatine, 1 $MgCl_2$, 10 HEPES, 0.2 EGTA, 4 Mg-ATP, 0.5 Na-GFP, pH adjusted to 7.25 with CsOH, 295 mOsm osmolarity. mIPSCs were isolated with 0.5 μM TTX, 50 μM APV (Tocris) and 20 μM DNQX (Tocris), and recorded from cells voltage clamped at −70 mV using high-Cl internal solution containing (in mM): 103 CsCl, 12 $CsMeSO_3$, 5 TEA-Cl, 10 HEPES, 4 Mg-ATP, 0.5 Na-GTP, 0.5 EGTA, 1 MgCl2, pH adjusted to 7.25 with CsOH, 295 mOsm osmolarity. Intrinsic excitability and passive membrane properties were recorded in the current clamp mode with the following internal solution (in mM): 130 K^+-D-gluconate, 10 KCl, 10 HEPES, 4 Mg-ATP, 0.5 Na-GTP, 0.2 EGTA, 1 MgCl2, pH adjusted to 7.25 with CsOH, 295 mOsm osmolarity. To determine the

excitability of cells, membrane potentials were measured in response to intracellular injection of step currents (500 ms duration, magnitudes ranging from −20 to 200 pA in steps of 20 pA). Data were collected using a Multiclamp 700B (Molecular Devices), filtered at 3 kHz and digitized at 10 kHz using a Digidata 1440A and Clampex 10.2 software (Molecular Devices). Recordings with access resistance greater than 30 MΩ or changes exceeding 15% were discarded.

To record evoked EPSCs (eEPSCs) from different excitatory pathways to the DG, stimulating theta glass pipettes (World Precision Instruments) with broken tips (~10–20 μm) were filled with ACSF and placed in the inner molecular layer (< 40 um from the border of the granule cell layer), middle molecular layer (middle third of the molecular layer) or outer molecular layer (outer third of the molecular layer) to stimulate different excitatory inputs onto DG granule cells (GCs). Bipolar square-wave voltage pulses (100–200 μs, 5–25 V) were delivered through a stimulus isolator (ISO-Flex, AMPI). Stimulation intensity was adjusted to obtain comparable amplitudes of AMPA eEPSCs (50–150 pA) across conditions. Paired whole-cell recordings were carried out on labeled (*F*-RAM$^+$ or *N*-RAM$^+$) and unlabeled neighboring neurons. Cells were first voltage clamped at −70 mV to record AMPA currents and paired pulses with a 100 ms interval were stimulated. The peak amplitude of the first pulse was used to calculate eEPSC amplitudes. The cells were subsequently voltage clamped at +40 mV and a single pulse was stimulated. NMDA currents were measured at 100 ms after the onset of stimulation. Values were averaged from 10 sweeps repeated every 20–30 seconds. Picrotoxin (50 μM) was added throughout the recording to block $GABA_A$ receptors. To confirm the specificity of stimulation, the mGluR2/3 agonist DCG-IV (1 μM) was routinely bath applied at the end of experiments, which reduced the amplitudes of eEPSCs selectively evoked by stimulating the MEC-DG pathway (medial perforant path, MPP).

To record optically evoked IPSCs (oIPSCs) or optically evoked EPSCs (oEPSCs) in the DG, 2 ms 470 nm LED stimulations at 0.1, 0.25, 0.50, 0.75, 1.00, 1.50 mW/mm^2, generated from a mounted LED (Thorlabs), were controlled by TTL input and delivered through the 40× objective. Paired whole-cell recordings were carried out on labeled (*F*-RAM$^+$ or *N*-RAM$^+$) and unlabeled neighboring neurons. oIPSCs were recorded in the presence of DNQX (20 μM) and APV (50 μM) from cells voltage clamped at 0 mV with Cs-based internal solution. In the experiments where CCK$^+$ interneurons were specifically stimulated, oIPSCs were recorded from cells voltage clamped at −70 mV with high-Cl internal solutions to minimize the effects of depolarization-induced suppression of inhibition (DSI) from CCK$^+$ interneurons. Average peak responses were calculated from 10 sweeps, stimulated every 10–15 seconds. Paired light pulses with an interval of 200 ms were given at 0.50 mW/mm^2 to measure paired-pulse ratios. To block transmission from individual interneuron subtypes, ω-agatoxin IVa (AgTx, 0.5 μM, Bachem), ω-conotoxin GVIa (CnTx, 1 μM, Bachem) or WIN 55,212–2 (WIN, 10 μM, Tocris) were bath applied in the ACSF during oIPSC recordings. oEPSCs were recorded in the presence of picrotoxin (50 μM), TTX (0.5 μM) and 4-aminopyridine (100 μM) from cells voltage clamped at −70 mV with Cs-based internal solution.

To characterize the CCK^+ interneurons, depolarization-induced suppression of inhibition (DSI) was induced by elevating the holding potential of the postsynaptic GCs from −70 mV to 0 mV for 5 seconds. oIPSCs were measured in GCs voltage clamped at −70 mV and recorded with high-Cl^- internal solution in the presence of APV (50 μM) and DNQX (20 μM). oIPSCs recorded before and 200 ms after depolarization, averaged from 10 sweeps, were used to calculate DSI. To examine asynchronous release from CCK^+ interneurons, trains of ten action potentials (50 Hz) were evoked in the presynaptic CCK^+ interneurons and unitary IPSCs (uIPSCs) recorded in the postsynaptic GCs voltage clamped at −70 mV. uIPSCs were also measured with WIN (10 μM) in the ACSF.

Data were analyzed using MiniAnalysis (Synaptosoft) and Clampfit 10.2 (Molecular Devices) by investigators that were blind to the experimental conditions.

Fiber photometry—A customized fiber photometry system was used. A 473 nm diode laser (OEM Laser Systems) was controlled by a function generator (Agilent, 33599B Series, 400 Hz, square wave). The light was coupled to a 400 μm 0.48 NA optical fiber (Thorlabs) using a 40× 0.65 NA microscope objective (Olympus) and a fiber launch (Thorlabs). Optical fiber with the same diameter was glued to a ceramic ferrule (Thorlabs) and implanted into the mice. Before experiments, implants were connected to the laser with ceramic split mating sleeves (Thorlabs). Laser intensity was set to a level that generates fluorescence signals of about 50% of the maximum detectable values. The GCaMP6f fluorescence signal was collected by the implanted optical fiber and passed through the objective and dichroic mirror. The signal was then transmitted through a longpass filter (Semrock) onto a NewFocus 2151 femtowatt silicon photoreceiver (Newport, DC High Mode). The photoreceiver was connected to a lock-in amplifier (SR830 DSP, Stanford Research Systems, 8 ms time constant) and data were recorded with customized LabVIEW software (National Instruments).

Fear conditioned animals were subjected to fiber photometry experiments 48 hours after training. On the testing day, after connecting their fiber implants, animals were allowed 10–20 minutes to recover in their home cages. Animals were then gently transferred from the home cage to context A, B or C and allowed free exploration for 4 minutes. Animals were then returned to their home cage and allowed to recover for 30 minutes before being transferred to the next context. The order of context exposure was randomized. GCaMP6f signal was collected throughout the experiment.

Fiber photometry data were analyzed with a custom MATLAB (MathWorks) program. Average ΔF/F signals over the entire 4-minute recall session were used to reflect neural activity. Signals were calculated as ΔF/F by normalizing the measured values during recall to the baseline fluorescence values. Baseline values were calculated as the median of the signals during the 60 seconds in the home cage prior to each context exposure. Signals recorded during physical transfer from the home cage to the contexts (30 seconds) were removed from the analysis.

Optogenetics—To optogenetically inhibit the MEC-DG pathway, animals were bilaterally implanted with optical fibers (Thorlabs) in the DG after viral injection into the MEC. After

CFC, animals were recalled in different contexts with optogenetic inhibition. Laser stimulation (561 nm, constant, 10 mW) was generated using a 561 nm DPSS laser (Opto Engine LLC) and delivered bilaterally to the DG through 200 μm 0.22 NA optical fibers (Thorlabs). A rotatory joint (Thorlabs) was used to allow animals to move freely. The laser was constantly on during the entire 4-minute recall session.

QUANTIFICATION AND STATISTICAL ANALYSIS

All statistical analyses were performed using Prism (GraphPad Software). Means of two groups were compared using either a Mann-Whitney test when the samples were not matched, or a Wilcoxon matched-pairs signed-rank test when the samples were matched. One-way ANOVA was used to compare group means between more than two groups, followed by either Dunnett's multiple comparisons test when all other groups were compared to the control group, or Tukey's multiple comparisons test when means of each pair of groups were compared. Two-way ANOVA was used to compare group means when there were two or more variables, followed by either Tukey's or Sidak's multiple comparisons tests (as noted in the figure legends). Depending on the experimental design, two-way ANOVA, two-way mixed ANOVA or two-way repeated measures ANOVA was used. A one-sample t-test was used to compare group means to hypothetical values. Linear regression was used to examine the correlation between two variables. All comparisons are two-sided. Statistical significance was determined as follows: *$p < 0.05$, **$p < 0.01$, ***$p < 0.001$. Data are shown as mean ± SEM. The statistical details of all experiments, including the number of samples, statistical tests, p values, can be found in Table S1.

DATA AND CODE AVAILABILITY

Data and custom MATLAB code are available upon request from the Lead Contact.

Supplementary Material

Refer to Web version on PubMed Central for supplementary material.

Acknowledgments:

We thank C. M. Fletcher and J. Radulovic for critical reading of the manuscript; M. Xu for providing *Fos*$^{flx/flx}$ mice; G. Fishell for sharing Dlx5/6 constructs; L. Paul, Y. Zhang, J. Xue, T.D. Yelhekar and F.-J. Weng for technical assistance; and W. Xu, D.S. Roy, P.E. Castillo, G. Vargish, E.LQ. Lee, J. Guo, and the entire Lin laboratory for helpful suggestions.

Funding: This work was funded by a Henry E. Singleton Fellowship, Leventhal Graduate Student Fellowship and Hugo Shong Fellowship (X.S.), Simons Postdoctoral Fellowship (S.R.), Beijing Municipal Science & Technology Commission (Z181100001518001, X.Z.), MIT Great China Fund for Innovation (Y.L. & X.Z.), NIH BRAIN Initiative 1R01MH111872 (P.O.A.), Solomon Buchsbaum Research Foundation Award and NIH grants MH091220, NS088421 and DC014701 (Y.L.). The authors declare no competing financial interests.

References

Amaral DG, and Witter MP (1989). The three-dimensional organization of the hippocampal formation: A review of anatomical data. Neuroscience 31, 571–591. [PubMed: 2687721]

Barth AL (2007). Visualizing circuits and systems using transgenic reporters of neural activity. Current opinion in neurobiology 17, 567–571. [PubMed: 18036810]

Barth AL, Gerkin RC, and Dean KL (2004). Alteration of neuronal firing properties after in vivo experience in a FosGFP transgenic mouse. The Journal of neuroscience : the official journal of the Society for Neuroscience 24, 6466–6475.

Bartos M, and Elgueta C (2012). Functional characteristics of parvalbumin- and cholecystokinin-expressing basket cells. J Physiol-London 590, 669–681. [PubMed: 22250212]

Bernier BE, Lacagnina AF, Ayoub A, Shue F, Zemelman BV, Krasne FB, and Drew MR (2017). Dentate Gyrus Contributes to Retrieval as well as Encoding: Evidence from Context Fear Conditioning, Recall, and Extinction. Journal of Neuroscience 37, 6359–6371. [PubMed: 28546308]

Cai DJ, Aharoni D, Shuman T, Shobe J, Biane J, Song W, Wei B, Veshkini M, La-Vu M, Lou J, et al. (2016). A shared neural ensemble links distinct contextual memories encoded close in time. Nature 534, 115–118. [PubMed: 27251287]

Castillo PE, Younts TJ, Chavez AE, and Hashimotodani Y (2012). Endocannabinoid Signaling and Synaptic Function. Neuron 76, 70–81. [PubMed: 23040807]

Chelaru MI, and Dragoi V (2008). Efficient coding in heterogeneous neuronal populations. Proceedings of the National Academy of Sciences of the United States of America 105, 16344–16349. [PubMed: 18854413]

Choi JH, Sim SE, Kim JI, Choi DI, Oh J, Ye S, Lee J, Kim T, Ko HG, Lim CS, et al. (2018). Interregional synaptic maps among engram cells underlie memory formation. Science 360, 430–435. [PubMed: 29700265]

Danielson NB, Turi GF, Ladow M, Chavlis S, Petrantonakis PC, Poirazi P, and Losonczy A (2017). In Vivo Imaging of Dentate Gyrus Mossy Cells in Behaving Mice. Neuron 93, 552-+. [PubMed: 28132825]

Deng W, Mayford M, and Gage FH (2013). Selection of distinct populations of dentate granule cells in response to inputs as a mechanism for pattern separation in mice. eLife 2, e00312. [PubMed: 23538967]

Denny CA, Kheirbek MA, Alba EL, Tanaka KF, Brachman RA, Laughman KB, Tomm NK, Turi GF, Losonczy A, and Hen R (2014). Hippocampal memory traces are differentially modulated by experience, time, and adult neurogenesis. Neuron 83, 189–201. [PubMed: 24991962]

Diehl GW, Hon OJ, Leutgeb S, and Leutgeb JK (2017). Grid and Nongrid Cells in Medial Entorhinal Cortex Represent Spatial Location and Environmental Features with Complementary Coding Schemes. Neuron 94, 83–92.e86. [PubMed: 28343867]

Dimidschstein J, Chen Q, Tremblay R, Rogers SL, Saldi GA, Guo L, Xu Q, Liu R, Lu C, Chu J, et al. (2016). A viral strategy for targeting and manipulating interneurons across vertebrate species. Nature neuroscience.

Dunsmoor JE, and Paz R (2015). Fear Generalization and Anxiety: Behavioral and Neural Mechanisms. Biological psychiatry 78, 336–343. [PubMed: 25981173]

Eichenbaum H (2004). Hippocampus: cognitive processes and neural representations that underlie declarative memory. Neuron 44, 109–120. [PubMed: 15450164]

Flavell SW, and Greenberg ME (2008). Signaling mechanisms linking neuronal activity to gene expression and plasticity of the nervous system. Annual review of neuroscience 31, 563–590.

Fleischmann A, Hvalby O, Jensen V, Strekalova T, Zacher C, Layer LE, Kvello A, Reschke M, Spanagel R, Sprengel R, et al. (2003). Impaired long-term memory and NR2A-type NMDA receptor-dependent synaptic plasticity in mice lacking c-Fos in the CNS. The Journal of neuroscience : the official journal of the Society for Neuroscience 23, 9116–9122.

Frankland PW, Cestari V, Filipkowski RK, McDonald RJ, and Silva AJ (1998). The dorsal hippocampus is essential for context discrimination but not for contextual conditioning. Behavioral Neuroscience 112, 863–874. [PubMed: 9733192]

Freund TF, and Buzsaki G (1996). Interneurons of the hippocampus. Hippocampus 6, 347–470. [PubMed: 8915675]

Fyhn M, Hafting T, Treves A, Moser MB, and Moser EI (2007). Hippocampal remapping and grid realignment in entorhinal cortex. Nature 446, 190–194. [PubMed: 17322902]

Garner AR, Rowland DC, Hwang SY, Baumgaertel K, Roth BL, Kentros C, and Mayford M (2012). Generation of a synthetic memory trace. Science 335, 1513–1516. [PubMed: 22442487]

Ghandour K, Ohkawa N, Fung CCA, Asai H, Saitoh Y, Takekawa T, Okubo-Suzuki R, Soya S, Nishizono H, Matsuo M, et al. (2019). Orchestrated ensemble activities constitute a hippocampal memory engram. Nature communications 10, 2637.

GoodSmith D, Chen XJ, Wang C, Kim SH, Song HJ, Burgalossi A, Christian KM, and Knierim JJ (2017). Spatial Representations of Granule Cells and Mossy Cells of the Dentate Gyrus. Neuron 93, 677-+. [PubMed: 28132828]

Grewe BF, Grundemann J, Kitch LJ, Lecoq JA, Parker JG, Marshall JD, Larkin MC, Jercog PE, Grenier F, Li JZ, et al. (2017). Neural ensemble dynamics underlying a long-term associative memory. Nature 543, 670-+. [PubMed: 28329757]

Grosmark AD, and Buzsáki G (2016). Diversity in neural firing dynamics supports both rigid and learned hippocampal sequences. Science 351, 1440–1443. [PubMed: 27013730]

Grosso A, Santoni G, Manassero E, Renna A, and Sacchetti B (2018). A neuronal basis for fear discrimination in the lateral amygdala. Nature communications 9.

Guenthner CJ, Miyamichi K, Yang HH, Heller HC, and Luo L (2013). Permanent genetic access to transiently active neurons via TRAP: targeted recombination in active populations. Neuron 78, 773–784. [PubMed: 23764283]

Guo NN, Soden ME, Herber C, Kim MT, Besnard A, Lin PY, Ma X, Cepko CL, Zweifel LS, and Sahay A (2018). Dentate granule cell recruitment of feedforward inhibition governs engram maintenance and remote memory generalization. Nat Med 24, 438-+. [PubMed: 29529016]

Guzowski JF, Timlin JA, Roysam B, McNaughton BL, Worley PF, and Barnes CA (2005). Mapping behaviorally relevant neural circuits with immediate-early gene expression. Current opinion in neurobiology 15, 599–606. [PubMed: 16150584]

Hainmueller T, and Bartos M (2018). Parallel emergence of stable and dynamic memory engrams in the hippocampus. Nature.

Hales JB, Schlesiger MI, Leutgeb JK, Squire LR, Leutgeb S, and Clark RE (2014). Medial Entorhinal Cortex Lesions Only Partially Disrupt Hippocampal Place Cells and Hippocampus-Dependent Place Memory. Cell reports 9, 893–901. [PubMed: 25437546]

Han JH, Kushner SA, Yiu AP, Hsiang HL, Buch T, Waisman A, Bontempi B, Neve RL, Frankland PW, and Josselyn SA (2009). Selective erasure of a fear memory. Science 323, 1492–1496. [PubMed: 19286560]

Hartzell AL, Martyniuk KM, Brigidi GS, Heinz DA, Djaja NA, Payne A, and Bloodgood BL (2018). NPAS4 recruits CCK basket cell synapses and enhances cannabinoid-sensitive inhibition in the mouse hippocampus. eLife 7.

Hashimotodani Y, Nasrallah K, Jensen KR, Chavez AE, Carrera D, and Castillo PE (2017). LTP at Hilar Mossy Cell-Dentate Granule Cell Synapses Modulates Dentate Gyrus Output by Increasing Excitation/Inhibition Balance. Neuron 95, 928-+. [PubMed: 28817805]

Hefft S, and Jonas P (2005). Asynchronous GABA release generates long-lasting inhibition at a hippocampal interneuron-principal neuron synapse. Nature neuroscience 8, 1319–1328. [PubMed: 16158066]

Herry C, Ciocchi S, Senn V, Demmou L, Muller C, and Luthi A (2008). Switching on and off fear by distinct neuronal circuits. Nature 454, 600–606. [PubMed: 18615015]

Hess J, Angel P, and Schorpp-Kistner M (2004). AP-1 subunits: quarrel and harmony among siblings. Journal of cell science 117, 5965–5973. [PubMed: 15564374]

Huckleberry KA, Ferguson LB, and Drew MR (2016). Behavioral mechanisms of context fear generalization in mice. Learning & memory 23, 703–709. [PubMed: 27918275]

Jinde S, Zsiros V, Jiang Z, Nakao K, Pickel J, Kohno K, Belforte JE, and Nakazawa K (2012). Hilar mossy cell degeneration causes transient dentate granule cell hyperexcitability and impaired pattern separation. Neuron 76, 1189–1200. [PubMed: 23259953]

Josselyn SA, Kohler S, and Frankland PW (2015). Finding the engram. Nature reviews Neuroscience 16, 521–534. [PubMed: 26289572]

Jun JK, Miller P, Hernández A, Zainos A, Lemus L, Brody CD, and Romo R (2010). Heterogenous Population Coding of a Short-Term Memory and Decision Task. The Journal of Neuroscience 30, 916. [PubMed: 20089900]

Kanter BR, Lykken CM, Avesar D, Weible A, Dickinson J, Dunn B, Borgesius NZ, Roudi Y, and Kentros CG (2017). A Novel Mechanism for the Grid-to-Place Cell Transformation Revealed by Transgenic Depolarization of Medial Entorhinal Cortex Layer II. Neuron 93, 1480-+. [PubMed: 28334610]

Kawashima T, Kitamura K, Suzuki K, Nonaka M, Kamijo S, Takemoto-Kimura S, Kano M, Okuno H, Ohki K, and Bito H (2013). Functional labeling of neurons and their projections using the synthetic activity-dependent promoter E-SARE. Nature methods 10, 889–895. [PubMed: 23852453]

Kawashima T, Okuno H, and Bito H (2014). A new era for functional labeling of neurons: activity-dependent promoters have come of age. Frontiers in neural circuits 8.

Kheirbek MA, Drew LJ, Burghardt NS, Costantini DO, Tannenholz L, Ahmari SE, Zeng H, Fenton AA, and Hen R (2013). Differential control of learning and anxiety along the dorsoventral axis of the dentate gyrus. Neuron 77, 955–968. [PubMed: 23473324]

Kheirbek MA, Klemenhagen KC, Sahay A, and Hen R (2012). Neurogenesis and generalization: a new approach to stratify and treat anxiety disorders. Nature neuroscience 15, 1613–1620. [PubMed: 23187693]

Kitamura T, Sun C, Martin J, Kitch LJ, Schnitzer MJ, and Tonegawa S (2015). Entorhinal Cortical Ocean Cells Encode Specific Contexts and Drive Context-Specific Fear Memory. Neuron 87, 1317–1331. [PubMed: 26402611]

Knierim JJ, and Neunuebel JP (2016). Tracking the flow of hippocampal computation: Pattern separation, pattern completion, and attractor dynamics. Neurobiology of learning and memory 129, 38–49. [PubMed: 26514299]

Kuhn HG, DickinsonAnson H, and Gage FH (1996). Neurogenesis in the dentate gyrus of the adult rat: Age-related decrease of neuronal progenitor proliferation. Journal of Neuroscience 16, 2027–2033. [PubMed: 8604047]

Lacagnina AF, Brockway ET, Crovetti CR, Shue F, McCarty MJ, Sattler KP, Lim SC, Santos SL, Denny CA, and Drew MR (2019). Distinct hippocampal engrams control extinction and relapse of fear memory. Nature neuroscience 22, 753–761. [PubMed: 30936555]

Lee I, and Kesner RP (2004). Encoding versus retrieval of spatial memory: double dissociation between the dentate gyrus and the perforant path inputs into CA3 in the dorsal hippocampus. Hippocampus 14, 66–76. [PubMed: 15058484]

Leutgeb JK, Leutgeb S, Moser MB, and Moser EI (2007). Pattern separation in the dentate gyrus and CA3 of the hippocampus. Science 315, 961–966. [PubMed: 17303747]

Lin Y, Bloodgood BL, Hauser JL, Lapan AD, Koon AC, Kim TK, Hu LS, Malik AN, and Greenberg ME (2008). Activity-dependent regulation of inhibitory synapse development by Npas4. Nature 455, 1198–1204. [PubMed: 18815592]

Liu X, Ramirez S, Pang PT, Puryear CB, Govindarajan A, Deisseroth K, and Tonegawa S (2012). Optogenetic stimulation of a hippocampal engram activates fear memory recall. Nature 484, 381–385. [PubMed: 22441246]

Lonergan ME, Gafford GM, Jarome TJ, and Helmstetter FJ (2010). Time-dependent expression of Arc and zif268 after acquisition of fear conditioning. Neural plasticity 2010, 139891. [PubMed: 20592749]

Macek TA, Winder DG, Gereau RW, Ladd CO, and Conn PJ (1996). Differential involvement of group II and group III mGluRs as autoreceptors at lateral and medial perforant path synapses. Journal of neurophysiology 76, 3798–3806. [PubMed: 8985877]

Mahan AL, and Ressler KJ (2012). Fear conditioning, synaptic plasticity and the amygdala: implications for posttraumatic stress disorder. Trends in neurosciences 35, 24–35. [PubMed: 21798604]

Mallory CS, and Giocomo LM (2018). Heterogeneity in hippocampal place coding. Current opinion in neurobiology 49, 158–167. [PubMed: 29522977]

McHugh TJ, Jones MW, Quinn JJ, Balthasar N, Coppari R, Elmquist JK, Lowell BB, Fanselow MS, Wilson MA, and Tonegawa S (2007). Dentate gyrus NMDA receptors mediate rapid pattern separation in the hippocampal network. Science 317, 94–99. [PubMed: 17556551]

Miao CL, Cao QC, Ito HT, Yamahachi H, Witter MP, Moser MB, and Moser EI (2015). Hippocampal Remapping after Partial Inactivation of the Medial Entorhinal Cortex. Neuron 88, 590–603. [PubMed: 26539894]

Mongiat LA, Esposito MS, Lombardi G, and Schinder AF (2009). Reliable Activation of Immature Neurons in the Adult Hippocampus. PloS one 4.

Nakashiba T, Cushman JD, Pelkey KA, Renaudineau S, Buhl DL, McHugh TJ, Rodriguez Barrera V, Chittajallu R, Iwamoto KS, McBain CJ, et al. (2012). Young dentate granule cells mediate pattern separation, whereas old granule cells facilitate pattern completion. Cell 149, 188–201. [PubMed: 22365813]

Nakayama D, Iwata H, Teshirogi C, Ikegaya Y, Matsuki N, and Nomura H (2015). Long-delayed expression of the immediate early gene Arc/Arg3.1 refines neuronal circuits to perpetuate fear memory. The Journal of neuroscience : the official journal of the Society for Neuroscience 35, 819–830. [PubMed: 25589774]

Osborne LC, Palmer SE, Lisberger SG, and Bialek W (2008). The neural basis for combinatorial coding in a cortical population response. The Journal of neuroscience : the official journal of the Society for Neuroscience 28, 13522–13531. [PubMed: 19074026]

Park S, Kramer EE, Mercaldo V, Rashid AJ, Insel N, Frankland PW, and Josselyn SA (2016). Neuronal Allocation to a Hippocampal Engram. Neuropsychopharmacology : official publication of the American College of Neuropsychopharmacology.

Pelkey KA, Chittajallu R, Craig MT, Tricoire L, Wester JC, and McBain CJ (2017). Hippocampal Gabaergic Inhibitory Interneurons. Physiol Rev 97, 1619–1747. [PubMed: 28954853]

Petersen RP, Moradpour F, Eadie BD, Shin JD, Kannangara TS, Delaney KR, and Christie BR (2013). Electrophysiological Identification of Medial and Lateral Perforant Path Inputs to the Dentate Gyrus. Neuroscience 252, 154–168. [PubMed: 23933307]

Pignatelli M, Ryan TJ, Roy DS, Lovett C, Smith LM, Muralidhar S, and Tonegawa S (2018). Engram Cell Excitability State Determines the Efficacy of Memory Retrieval. Neuron.

Ramamoorthi K, Fropf R, Belfort GM, Fitzmaurice HL, McKinney RM, Neve RL, Otto T, and Lin Y (2011). Npas4 regulates a transcriptional program in CA3 required for contextual memory formation. Science 334, 1669–1675. [PubMed: 22194569]

Reijmers LG, Perkins BL, Matsuo N, and Mayford M (2007). Localization of a stable neural correlate of associative memory. Science 317, 1230–1233. [PubMed: 17761885]

Richter FR, Cooper RA, Bays PM, and Simons JS (2016). Distinct neural mechanisms underlie the success, precision, and vividness of episodic memory. eLife 5.

Roth BL (2016). DREADDs for Neuroscientists. Neuron 89, 683–694. [PubMed: 26889809]

Rozeske RR, Jercog D, Karalis N, Chaudun F, Khoder S, Girard D, Winke N, and Herry C (2018). Prefrontal-Periaqueductal Gray-Projecting Neurons Mediate Context Fear Discrimination. Neuron 97, 898-+. [PubMed: 29398355]

Ryan TJ, Roy DS, Pignatelli M, Arons A, and Tonegawa S (2015). Engram cells retain memory under retrograde amnesia. Science 348, 1007–1013. [PubMed: 26023136]

Scharfman HE, and Myers CE (2013). Hilar mossy cells of the dentate gyrus: a historical perspective. Frontiers in neural circuits 6.

Senzai Y, and Buzsaki G (2017). Physiological Properties and Behavioral Correlates of Hippocampal Granule Cells and Mossy Cells. Neuron 93, 691-+. [PubMed: 28132824]

Sørensen AT, Cooper YA, Baratta MV, Weng F-J, Zhang Y, Ramamoorthi K, Fropf R, LaVerriere E, Xue J, Young A, et al. (2016). A robust activity marking system for exploring active neuronal ensembles. eLife 5, e13918. [PubMed: 27661450]

Sun X, and Lin Y (2016). Npas4: Linking Neuronal Activity to Memory. Trends in neurosciences 39, 264–275. [PubMed: 26987258]

Tanaka KZ, He HS, Tomar A, Niisato K, Huang AJY, and McHugh TJ (2018). The hippocampal engram maps experience but not place. Science 361, 392–397. [PubMed: 30049878]

Tanaka KZ, and McHugh TJ (2018). The Hippocampal Engram as a Memory Index. Journal of experimental neuroscience 12, 1179069518815942. [PubMed: 30546263]

Tanaka KZ, Pevzner A, Hamidi AB, Nakazawa Y, Graham J, and Wiltgen BJ (2014). Cortical representations are reinstated by the hippocampus during memory retrieval. Neuron 84, 347–354. [PubMed: 25308331]

Taniguchi H, He M, Wu P, Kim S, Paik R, Sugino K, Kvitsani D, Fu Y, Lu J, Lin Y, et al. (2011). A Resource of Cre Driver Lines for Genetic Targeting of GABAergic Neurons in Cerebral Cortex. Neuron 71, 995–1013. [PubMed: 21943598]

Thompson RF (2005). In search of memory traces. Annual review of psychology 56, 1–23.

Tonegawa S, Liu X, Ramirez S, and Redondo R (2015). Memory Engram Cells Have Come of Age. Neuron 87, 918–931. [PubMed: 26335640]

Treves A, and Rolls ET (1994). Computational Analysis of the Role of the Hippocampus in Memory. Hippocampus 4, 374–391. [PubMed: 7842058]

Tsou K, Mackie K, Sanudo-Pena MC, and Walker JM (1999). Cannabinoid CB1 receptors are localized primarily on cholecystokinin-containing gabaergic interneurons in the rat hippocampal formation. Neuroscience 93, 969–975. [PubMed: 10473261]

van Dijk MT, and Fenton AA (2018). On How the Dentate Gyrus Contributes to Memory Discrimination. Neuron 98, 832-+. [PubMed: 29731252]

Weng F-J, Garcia RI, Lutzu S, Alviña K, Zhang Y, Dushko M, Ku T, Zemoura K, Rich D, Garcia-Dominguez D, et al. (2018). Npas4 Is a Critical Regulator of Learning-Induced Plasticity at Mossy Fiber-CA3 Synapses during Contextual Memory Formation. Neuron 97, 1137–1152.e1135. [PubMed: 29429933]

Wiltgen BJ, and Silva AJ (2007). Memory for context becomes less specific with time. Learning & memory 14, 313–317. [PubMed: 17522020]

Witter MP (2007). The perforant path: projections from the entorhinal cortex to the dentate gyrus. Prog Brain Res 163, 43–61. [PubMed: 17765711]

Xu W, and Sudhof TC (2013). A neural circuit for memory specificity and generalization. Science 339, 1290–1295. [PubMed: 23493706]

Yap E-L, and Greenberg ME (2018). Activity-Regulated Transcription: Bridging the Gap between Neural Activity and Behavior. Neuron 100, 330–348. [PubMed: 30359600]

Yiu AP, Mercaldo V, Yan C, Richards B, Rashid AJ, Hsiang HL, Pressey J, Mahadevan V, Tran MM, Kushner SA, et al. (2014). Neurons are recruited to a memory trace based on relative neuronal excitability immediately before training. Neuron 83, 722–735. [PubMed: 25102562]

Yokose J, Okubo-Suzuki R, Nomoto M, Ohkawa N, Nishizono H, Suzuki A, Matsuo M, Tsujimura S, Takahashi Y, Nagase M, et al. (2017). Overlapping memory trace indispensable for linking, but not recalling, individual memories. Science 355, 398–403. [PubMed: 28126819]

Zhao R, Grunke SD, Keralapurath MM, Yetman MJ, Lam A, Lee TC, Sousounis K, Jiang YY, Swing DA, Tessarollo L, et al. (2016). Impaired Recall of Positional Memory following Chemogenetic Disruption of Place Field Stability. Cell reports 16, 793–804. [PubMed: 27373150]

Zhou Y, Won J, Karlsson MG, Zhou M, Rogerson T, Balaji J, Neve R, Poirazi P, and Silva AJ (2009). CREB regulates excitability and the allocation of memory to subsets of neurons in the amygdala. Nature neuroscience 12, 1438–1443. [PubMed: 19783993]

Highlights

- Functionally distinct neuronal ensembles exist within a single memory engram
- *Fos*- and *Npas4*-dependent ensembles undergo distinct synaptic modifications after CFC
- *Fos*- and *Npas4*-dependent ensembles drive memory-guided behaviors in opposite directions
- Memory generalization and discrimination respectively require MEC and CCK^+ interneurons

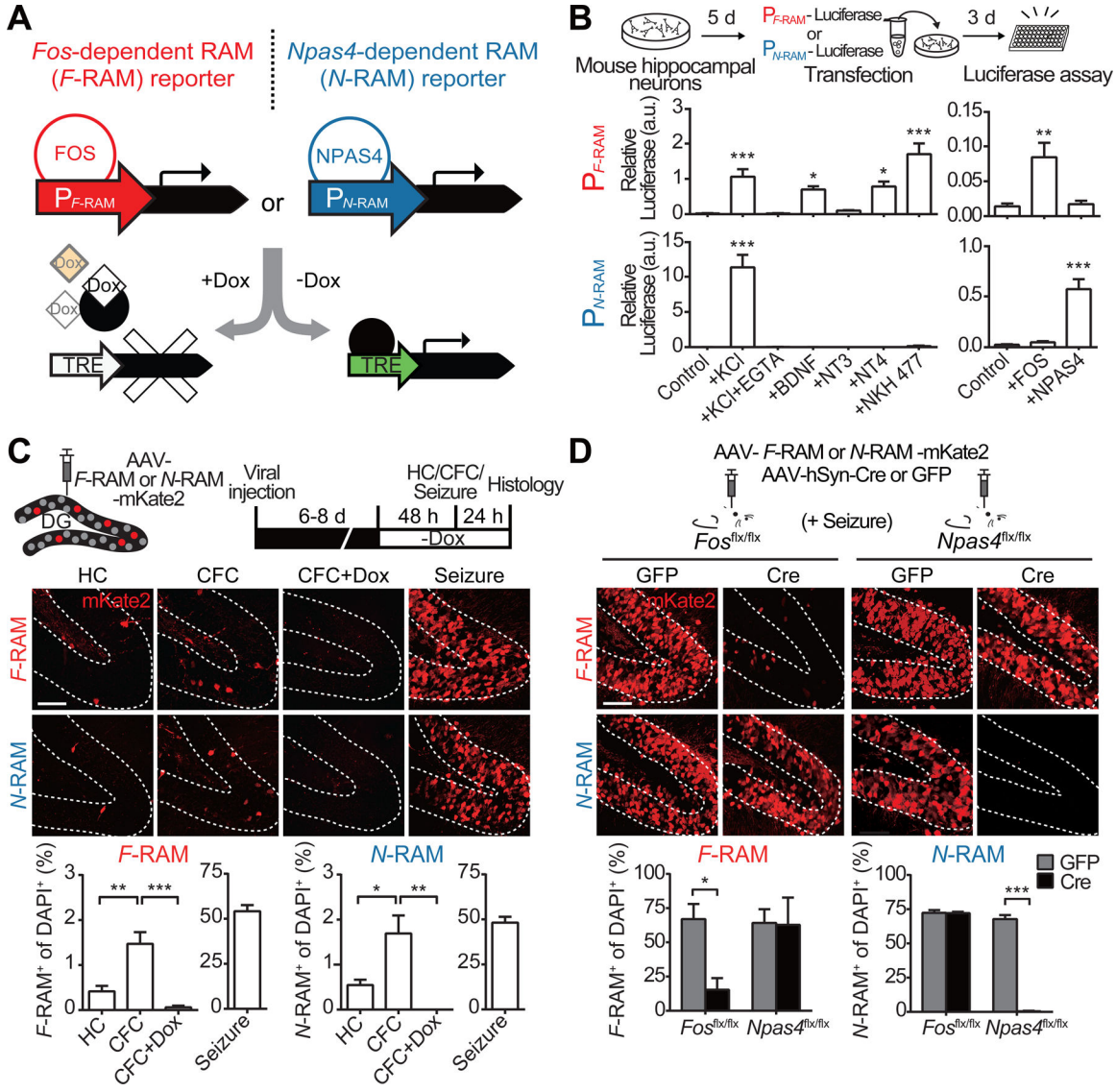

Figure 1. The *F*-RAM and *N*-RAM Reporters Selectively Capture *Fos*- and *Npas4*-dependent Neuronal Ensembles.

(A) Design of the *F*-RAM and *N*-RAM reporters.

(B) Characterization of $P_{F\text{-RAM}}$ and $P_{N\text{-RAM}}$. Cultured hippocampal neurons were transfected with luciferase expression plasmids and treated with various extracellular stimuli. The induction of $P_{F\text{-RAM}}$ or $P_{N\text{-RAM}}$ by various extracellular stimuli was measured by luciferase assay. One-way ANOVA, Dunnett's test, n = 8–9.

(C) *F*-RAM and *N*-RAM label experience-activated neuronal ensembles *in vivo*. Representative images of the dorsal DG granule cell layers (GCL, dashed lines) and quantifications showing ensembles labeled under the home cage (HC), contextual fear conditioning (CFC), CFC but on Dox (CFC+Dox), and seizure conditions. One-way ANOVA, Tukey's test, n = 4 per condition.

(D) *F*-RAM and *N*-RAM are dependent on endogenous *Fos* and *Npas4*, respectively. Representative images and quantifications showing seizure-induced reporter activation in *Fos* and *Npas4* conditional knockout animals. Two-way ANOVA, Sidak's test, n = 3–4.

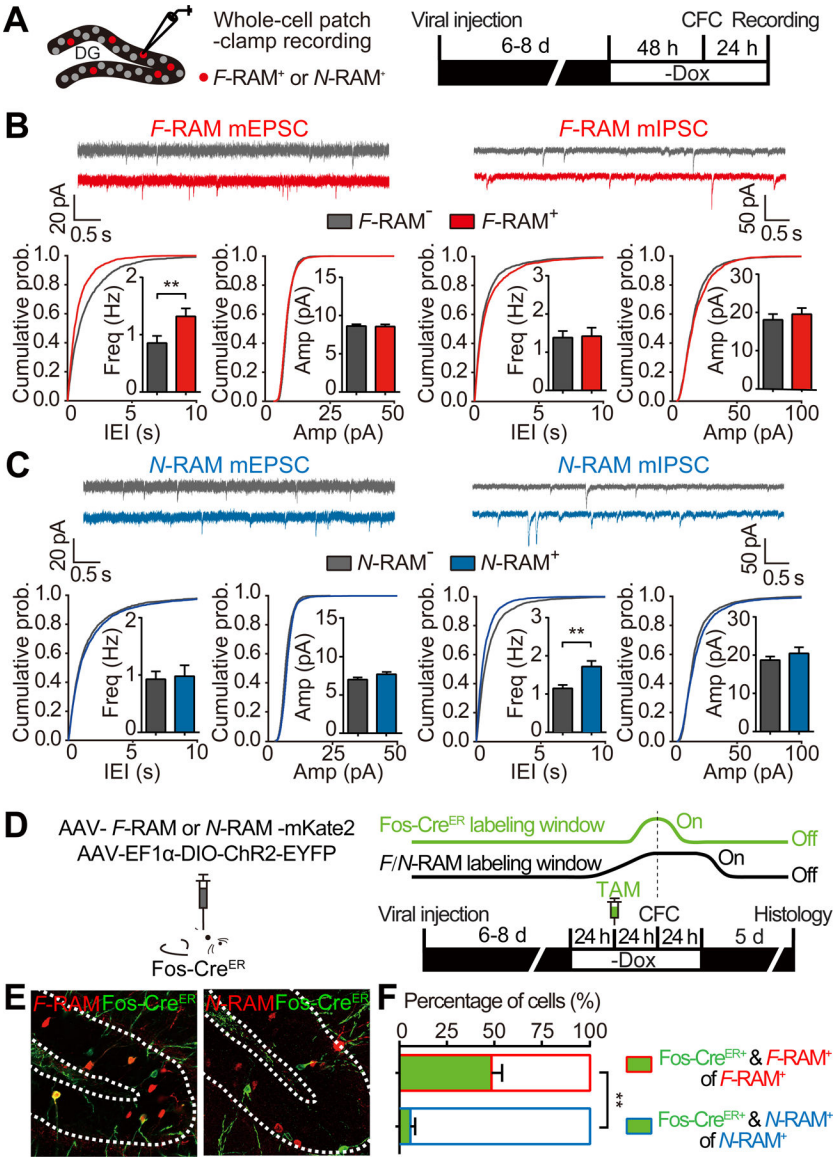

Figure 2. The *F*-RAM and *N*-RAM Ensembles are Distinct Neuronal Populations with Distinct Synaptic Properties.

(A) Experimental scheme to measure mEPSCs and mIPSCs on labeled *F*-RAM$^+$ or *N*-RAM$^+$ neurons and unlabeled neighboring neurons.

(B) *F*-RAM$^+$ neurons showed increased mEPSC frequency (Mann-Whitney test; *F*-RAM$^-$, n = 17; *F*-RAM$^+$, n = 17) but unchanged mIPSCs (n = 18, 19).

(C) *N*-RAM$^+$ neurons showed unchanged mEPSCs (*N*-RAM$^-$, n = 20; *N*-RAM$^+$, n = 20), but increased mIPSC frequency (n = 25, 26).

(D) Experimental scheme to co-label the *F*-RAM or *N*-RAM and Fos-Cre^{ER} ensembles in Fos-Cre^{ER} mice. Dox was removed 48 hours before CFC to label the *F*-RAM or *N*-RAM ensemble (black line). Tamoxifen (TAM) was injected i.p. 24 hours before CFC to label the Fos-Cre^{ER} ensemble (green line).

(E and F) Representative images (E) and quantification (F) showing overlap between the *F*-RAM or *N*-RAM and Fos-Cre^{ER} ensembles. Mann-Whitney test, n = 5 per group.

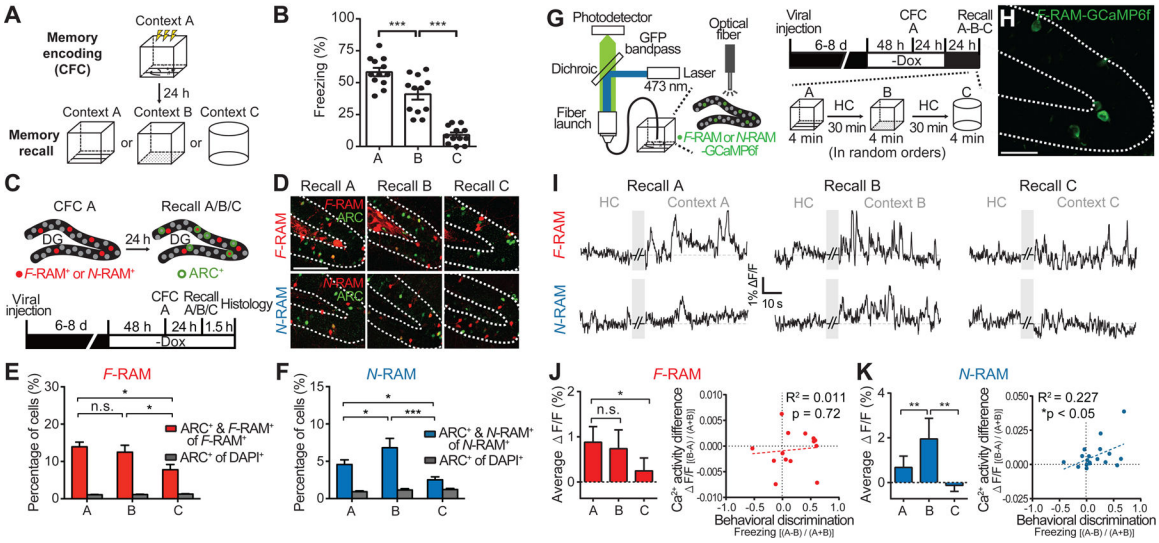

Figure 3. The *F*-RAM and *N*-RAM Ensembles Show Distinct Activity Patterns During the Contextual Fear Memory Discrimination-Generalization Assay.

(A) Schematic of the behavioral assay.

(B) Freezing levels during memory recall in the three contexts. One-way ANOVA, Tukey's test, n = 12 per group.

(C) Experimental scheme to identify recall-activated *F*-RAM and *N*-RAM ensemble neurons using *Arc* expression (ARC$^+$).

(D) Representative images showing overlap (white arrows) of the labeled *F*-RAM$^+$ or *N*-RAM$^+$ neurons and ARC$^+$ neurons.

(E and F) Percentages of the *F*-RAM$^+$ (E) and *N*-RAM$^+$ neurons (F) reactivated during memory recall. Two-way mixed ANOVA, Tukey's test, n = 7–9.

(G) Schematic and timeline for examination of Ca^{2+} activity in ensemble neurons using fiber photometry.

(H) Representative image showing the expression of GCaMP6f in the *F*-RAM ensemble after CFC.

(I) Representative traces showing Ca^{2+} activity in *F*-RAM$^+$ and *N*-RAM$^+$ neurons.

(J) Left, *F*-RAM ensemble activity (ΔF/F) during memory recall in different contexts (Friedman's one-way repeated measures ANOVA, Dunn's test, n = 14). Right, correlation between animal's ability to discriminate contexts A and B ($Freezing_{[(A-B)/(A+B)]}$) and the difference in *F*-RAM ensemble activities in these two contexts ($\Delta F/F_{[(B-A)/(A+B)]}$; linear regression, n = 14).

(K) The same as (J), except for *N*-RAM (n = 19).

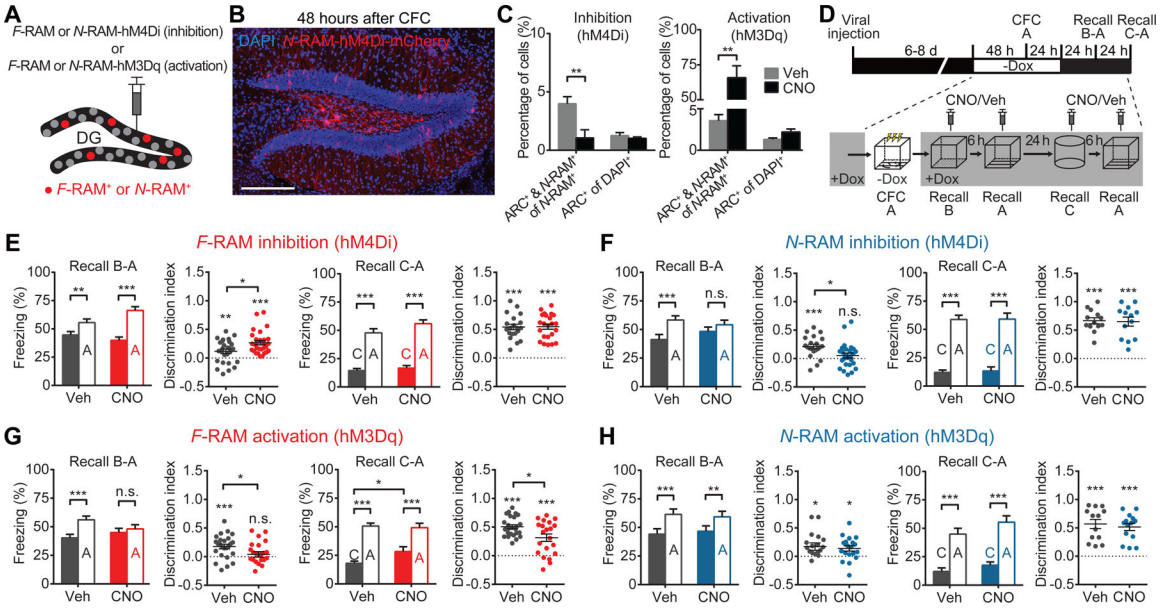

Figure 4. *F*-RAM and *N*-RAM Ensembles Oppositely Regulate the Memory Discrimination-Generalization Balance.

(A) Schematics for expression of hM4Di or hM3Dq in ensembles.

(B) Representative image showing expression of hM4Di-mCherry in the *N*-RAM ensemble.

(C) Percentages of ensemble neurons reactivated during memory recall, labeled by *Arc* expression (ARC^+), showing that hM4Di inhibited and hM3Dq activated ensemble neurons (two-way mixed ANOVA, Sidak's test, n = 5 per group).

(D) Experimental scheme to probe the functions of the *F*-RAM and *N*-RAM ensembles in memory discrimination-generalization.

(E) Inhibition of *F*-RAM ensembles enhanced discrimination between contexts A and B (Veh, n = 27; CNO, n = 29), but not A and C (n = 20, 23). Discrimination indices are calculated as $Freezing_{[(A-B)/(A+B)]}$ or $Freezing_{[(A-C)/(A+C)]}$.

(F) Inhibition of *N*-RAM ensembles reduced discrimination between contexts A and B (n = 21, 26), but not A and C (n = 13, 13).

(G) Activation of *F*-RAM ensembles reduced discrimination between contexts A and B (n = 25, 23), and between A and C (n = 21, 25).

(H) Activation of *N*-RAM ensembles did not affect discrimination between contexts A and B (n = 18, 19), or A and C (n = 13, 14).

Two-way mixed ANOVA with Sidak's test was used for freezing levels, Mann-Whitney test for comparing discrimination indices, and one-sample t-test to compare discrimination indices with zero.

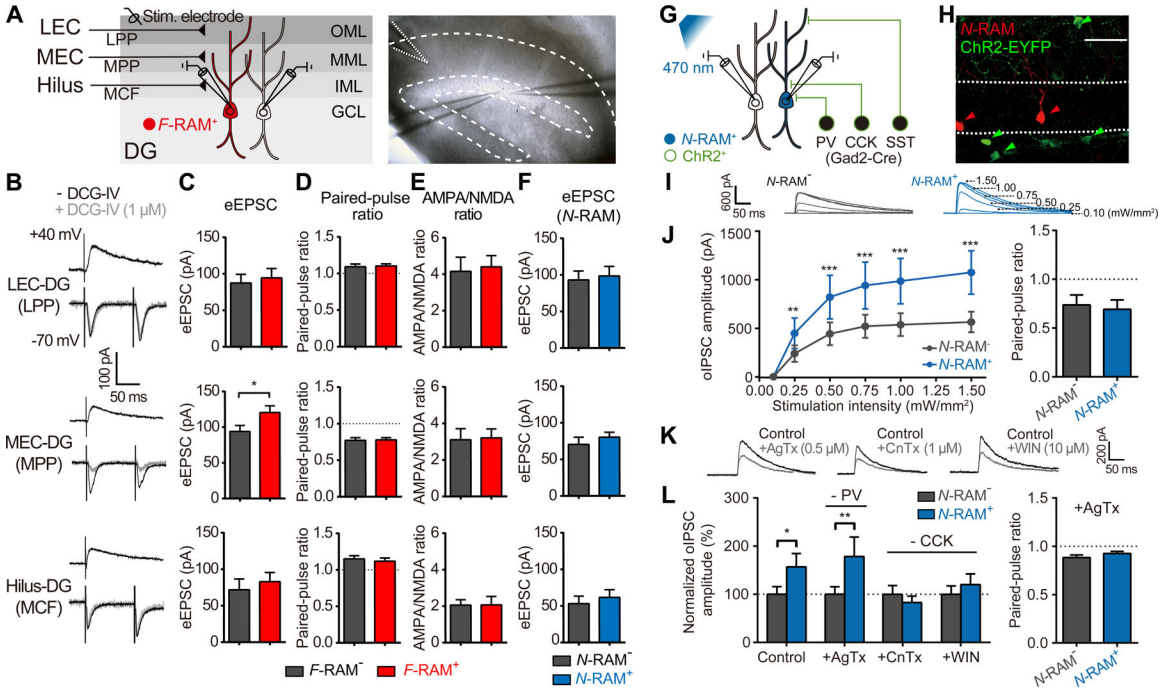

Figure 5. The *F*-RAM Ensemble Receives Increased Excitatory Inputs from the MEC and the *N*-RAM Ensemble Receives Enhanced Inhibitory Inputs from DG CCK$^+$ Interneurons

(A) Left, experimental scheme for simultaneous recording of eEPSCs, elicited by stimulating the LPP, MPP or MCF, on pairs of *F*-RAM$^+$ or *N*-RAM$^+$ neurons and nearby unlabeled neurons. Right, representative image of MPP stimulation.

(B) Representative traces of eEPSCs during LPP, MPP and MCF stimulation. Grey traces denote eEPSCs in the presence of DCG-IV.

(C-E) Bar graphs comparing eEPSC amplitudes (C, Wilcoxon signed-rank test, n = 15, 18, 21 pairs for LPP, MPP and MCF, respectively), paired-pulse ratios (D, n = 18, 20, 13) and AMPA/NMDA ratios (E, n = 15, 19, 13) between pairs of *F*-RAM$^+$ and *F*-RAM$^-$ neurons.

(F) Bar graph comparing eEPSC amplitudes between pairs of *N*-RAM$^+$ and *N*-RAM$^-$ neurons (n = 10, 13, 11).

(G) Experimental scheme for simultaneous recording of oIPSCs on pairs of *N*-RAM$^+$ or *F*-RAM$^+$ and nearby unlabeled neurons. oIPSCs were elicited by optogenetically stimulating ChR2-expressing GABAergic interneurons in Gad2-Cre mice.

(H) Representative image showing *N*-RAM and ChR2 expression.

(I) Representative traces showing oIPSCs recorded in pairs of nearby *N*-RAM$^+$ and *N*-RAM$^-$ neurons.

(J) Comparison of oIPSC amplitudes (left; two-way repeated measures ANOVA, Sidak's test, n = 10 pairs) and paired-pulse ratios (right; 200 ms interval, 0.50 mW/mm^2, Wilcoxon signed-rank test, n = 10) between *N*-RAM$^+$ and *N*-RAM$^-$ neurons.

(K) Representative traces showing that oIPSC amplitudes were reduced with bath application of AgTx, CnTx and WIN.

(L) Left, oIPSC amplitudes in *N*-RAM$^+$ and *N*-RAM$^-$ neurons with and without blockers (two-way mixed ANOVA, Sidak's test, n = 16, 10, 12, 13 pairs for control, AgTx, CnTx and WIN). Right, paired-pulse ratios in the presence of AgTx (n = 12).

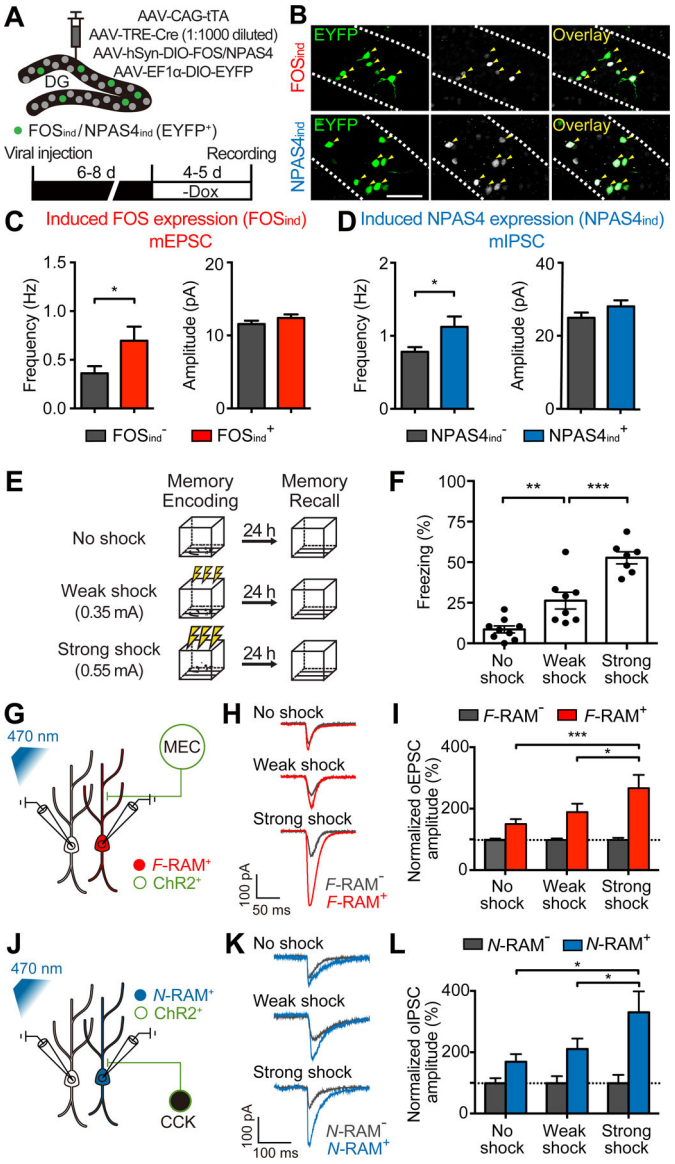

Figure 6. Synaptic Changes on Ensemble Neurons Are Correlated with the Strength of Learning.

(A) Experimental scheme for inducing FOS or NPAS4 expression in sparse and randomly selected DG neurons.

(B) Representative images showing induced FOS or NPAS4 expression (FOS_{ind} or $NPAS4_{ind}$) in randomly selected neurons ($EYFP^+$, white arrows).

(C) FOS_{ind} increased mEPSC frequency (Mann-Whitney test; $EYFP^-$, n = 19; $EYFP^+$, n = 20).

(D) $NPAS4_{ind}$ increased mIPSC frequency (n = 19, 20).

(E and F) Experimental scheme (E) showing that training of animals in context A with no shock, weak (0.35 mA) or strong shock (0.55 mA) resulted in different memory strengths, as indicated by levels of freezing (F; one-way ANOVA, Tukey's test, n = 7–9).

(G and H) Experimental scheme (G) and representative traces (H) showing simultaneous recording of oEPSCs on *F*-RAM$^+$ and *F*-RAM$^-$ cells with optogenetic stimulation of the MEC inputs.

(I) *F*-RAM$^+$ cells showed the largest oEPSC amplitudes in the strong shock group (two-way mixed ANOVA, Tukey's test, n = 24, 28, 21 pairs for no shock, weak shock and strong shock, respectively).

(J and K) Experimental scheme (J) and representative traces (K) showing simultaneous recording of oIPSCs on *N*-RAM$^+$ and *N*-RAM$^-$ cells with optogenetic stimulation of the CCK$^+$ interneurons.

(L) *N*-RAM$^+$ cells showed the largest oIPSC amplitudes in the strong shock group (n = 19, 15, 9).

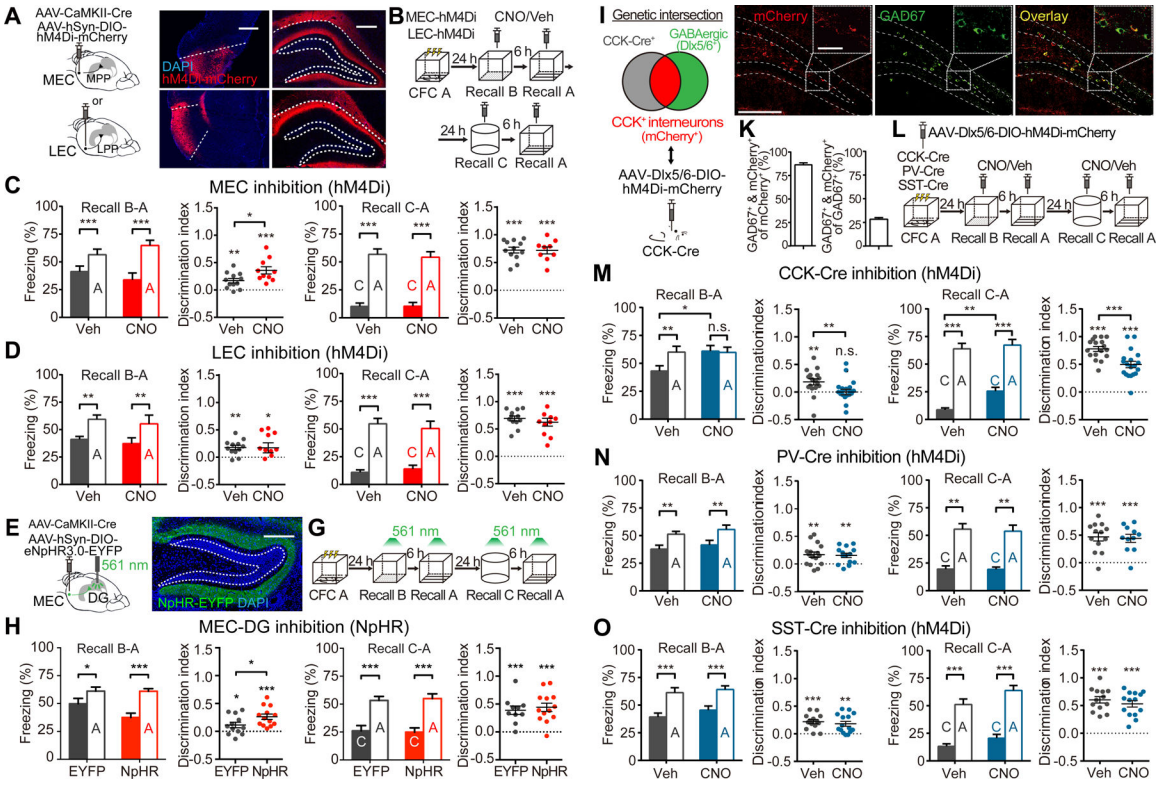

Figure 7. The MEC-DG Pathway Mediates Memory Generalization and DG CCK$^+$ Interneurons Mediate Memory Discrimination.

(A) Schematics and representative images showing selective expression of hM4Di in MEC and LEC projection neurons, which send their axonal terminals to the DG MML or OML, respectively.

(B) Experimental scheme for inhibition of MEC or LEC during memory discrimination-generalization.

(C) Inhibiting the MEC enhanced discrimination between contexts A and B (Veh, n = 12; CNO, n = 10), but not A and C (n = 12, 9).

(D) Inhibiting the LEC did not affect generalization between contexts A and B (n = 12, 11) or A and C (n = 12, 10).

(E and F) Schematic (E) and representative image (F) for selective expression of NpHR in MEC projection neurons, which project to the MML of the DG.

(G) Experimental scheme to optogenetically inhibit the MEC-DG pathway during memory recall with 561 nm constant light.

(H) Inhibition of the MEC-DG pathway enhanced discrimination between contexts A and B (EYFP, n = 12; NpHR, n = 13), but not between contexts A and C (n = 10, 13).

(I) Genetic intersection strategy to target CCK$^+$ GABAergic interneurons in DG.

(J) Representative images showing co-localization (white arrows) of labeled cells (mCherry$^+$) with GAD67.

(K) Quantifications showing that labeled neurons were mostly GABAergic (GAD67$^+$) and made up 28% of the GABAergic interneurons in the DG (n = 3).

(L) Experimental scheme to determine which interneuron subtypes are involved in memory discrimination-generalization.

(M) Inhibiting CCK^+ interneurons in the DG reduced discrimination between contexts A and B (Veh, n = 17; CNO, n = 20), and between A and C (n = 17, 19).
(N and O) Discrimination was not affected by inhibiting PV^+ interneurons (N, A and B: n = 16, 14; A and C: n = 13, 11) or SST^+ interneurons (O, A and B: n = 14, 15; A and C: n = 13, 14).
Two-way mixed ANOVA with Sidak's test was used for freezing levels, Mann-Whitney test for comparing discrimination indices, and one-sample t-test to compare discrimination indices with zero.